CZECH TECHNICAL UNIVERSITY IN PRAGUE

Faculty of Nuclear Sciences and Physical Engineering

Department of Physics

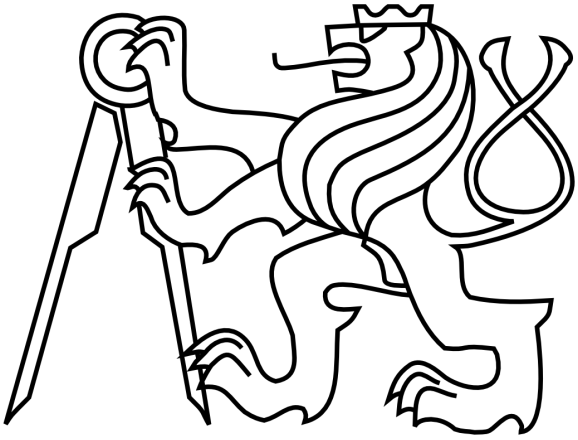

Diploma thesis

Measurement of dijet angular correlation in pp collisions in the ATLAS experiment

Bc. Vladimír Žitka

Supervisor: Ing. Miroslav Myška, Ph.D.

Consultant: Ing. Zdeněk Hubáček, Ph.D.

Prague, 2019

České vysoké učení technické v Praze

Fakulta jaderná a fyzikálně inženýrská

Katedra fyziky

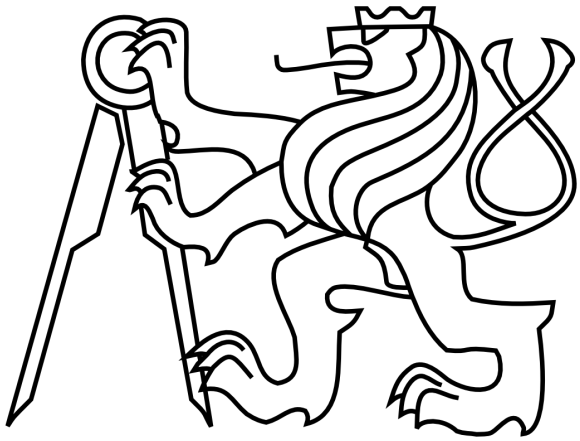

Diplomová práce

Měření úhlové korelace mezi dvěma jety v pp srážkách v experimentu ATLAS

Bc. Vladimír Žitka

Vedoucí práce: Ing. Miroslav Myška, Ph.D.

Konzultant: Ing. Zdeněk Hubáček, Ph.D.

Praha, 2019

Název práce:
Měření úhlové korelace mezi dvěma jety v pp srážkách v experimentu ATLAS

Autor: Vladimír Žitka
Obor: Experimentální jaderná a částicová fyzika
Druh práce: Diplomová práce
Vedoucí práce: Ing. Miroslav Myška, Ph.D., Katedra fyziky, Fakulta jaderná a fyzikálně inženýrská, České vysoké učení technické v Praze
Konzultant: Ing. Zdeněk Hubáček, Ph.D. , Katedra fyziky, Fakulta jaderná a fyzikálně inženýrská, České vysoké učení technické v Praze

Abstrakt:
Tato diplomová práce se zabývá precizním měřením silné interakce protonů při těžišťové energii 13 TeV v rámci experimentu ATLAS na urychlovači LHC. Práce podává komplexní přehled dosavadních výsledků experimentů nejen na LHC v oblasti jetové fyziky, speciální pozornost je věnována měření příčné hybnosti jetů v inkluzivní selekci a charakteristikám dijetových systémů. Vzhledem k dostatečnému množství dat jsou všechny proměnné měřené jako dvojitě diferenciální účinný průřez vzhledem k rapiditě jetu. V návaznosti na přechozí měření je pak poskytnut první náhled na data měřená detektorem ATLAS během roku 2018 Run II o celkové integrované luminositě 58.5 fb^{-1}.

Klíčová slova: ATLAS, dijety, azimutální korelace, silná vazbová konstanta

Title:

Measurement of dijet angular correlation in pp collisions in the ATLAS experiment

Author: Vladimír Žitka

Abstract:

This diploma thesis concerns the precision measurements of strong interactions of protons at the centre-of-mass energy of 13 TeV by the ATLAS experiment at the LHC. A complex overview of previous measurements not only from LHC experiments in the field of jet physics is provided, with special attention paid to the measurements of inclusive jet transverse momenta distributions and dijet system properties. Thanks to the amount of measured data all properties can be measured doubly-differentially with respect to jet rapidity. As a follow up to these measurements, a first look at the data measured by the ATLAS detector during the year 2018 of Run II with the integrated luminosity of 58.5 fb^{-1} is provided.

Keywords: ATLAS, dijets, azimuthal correlation, strong coupling

Prohlášení:

Prohlašuji, že jsem svou diplomovou práci vypracoval samostatně a použil jsem pouze podklady uvedené v přiloženém seznamu.

Nemám závažný důvod proti použití tohoto školního díla ve smyslu § 60 Zákona č. 121/2000 Sb., o právu autorském, o právech souvisejících s právem autorským a o změně některých zákonů (autorský zákon).

V Praze dne 6. 5. 2019 Vladimír Žitka

Poděkování:
Tímto bych chtěl poděkovat svému školiteli Miroslavu Myškovi a konzultantovi Zdeňku Hubáčkovi za jejich trpělivost, ochotu a expertízu při vedení mé práce. Dále bych chtěl poděkovat svým rodičům, kteří mě plně podporovali během celé doby mého studia. A nakonec bych chtěl poděkovat všem svým přátelům, kteří mi pomohli celým studiem projít bez ztráty zdravého rozumu a smyslu pro humor.

Contents

List of Figures

Introduction

The main intention of this diploma thesis is to inform the reader about the concept of dijet azimuthal correlation and its measurement. Firstly however, the Standard Model of particle physics and the measurement aperture has to be introduced, in order to be familiar with the terminology and techniques used during the analysis.

It is assumed, that most of kinematic variables and concepts are well known, but most of the used ones are defined when deemed appropriate and useful. Furthermore, it is assumed that basic concepts such as classifications of elementary particles and interactions are well known as well and so we provide only a brief overview at the start of the chapter two.

The first chapter is a brief overview of the ATLAS experiment, because this thesis is written in collaboration with the ATLAS Standard Model group and uses its data.

The second chapter concerns itself with and overview of Quantum Chromodynamis (QCD). It includes a section describing the structure of the proton and its influence on scattering experiments, due to the fact that for a long time proton was considered to be an elementary particle without an inner structure, similar to electron and the discovery of the contrary was a great step in particle physics research. The rest of the second chapter contains a foray into QCD itself and its properties such as running coupling or colour confinement.

The third chapter is a compilation of the experimental work done in this field up to date. It includes the measurements of inclusive transverse momentum spectra, dijet mass spectra, azimuthal correlations and one section is dedicated to the measurements of strong coupling using different techniques.

The fourth chapter contains an attempt to extend the previous measurements described in chapter three to the newest ATLAS data from the year 2018.

Chapter 1

The ATLAS detector

The Large Hadron Collider (LHC) at CERN is to this day the largest particle accelerator ever built. The circumference of the LHC is 27 km and it is housed in a tunnel approximately 100 m underground at the border of Switzerland and France. As of 2018, the maximum centre-of-mass energy in proton-proton collisions at the LHC is $\sqrt(s) = 13$ TeV. There are 4 major particle physics experiments at the LHC: ATLAS, ALICE, CMS and LHCb. Because this thesis analyzes data from the ATLAS detector, let us now present a brief overview of this experiment.

1.1 ATLAS

As is often the case with particle physics experiments, the name ATLAS is an acronym from: "A Toroidal LHC AparatuS". It is a multi-purpose particle detector that is forward-backward and azimuthally symmetric with respect to the interaction point.

Let us now describe the coordinate system and a few observables that are used throughout this thesis, unless stated otherwise. The origin of the coordinate system is defining the nominal interaction point, the beam direction defines the z-axis and the x-y plane is transverse to the beam direction. The positive x-axis is defined so that it points from interaction point to the centre of LHC ring and the y-axis points upwards. As per usual the azimuthal angle ϕ is measured around the beam axis and the polar angle Θ is the angle from the beam axis. The pseudorapidity is defined as $\eta = -\ln\tan(\frac{\Theta}{2})$ and the rapidity is defined as $y = \frac{1}{2}\ln[\frac{E+p_z}{E-p_z}]$. Furthermore all the transverse quantities (such as momentum, energy or missing energy) p_T, E_T and E_T^{miss} are defined in the $x-y$ plane unless stated otherwise.

A depiction of the ATLAS detector and its general layout is provided in Fig.1.1. The dimensions of ATLAS are: 25 m in height and 44 meters in length. The detector is conceptually divided into two region: barrel - the part of ATLAS that covers approximately the pseudorapidity up to 1.5 and end-cap - the part of ATLAS that

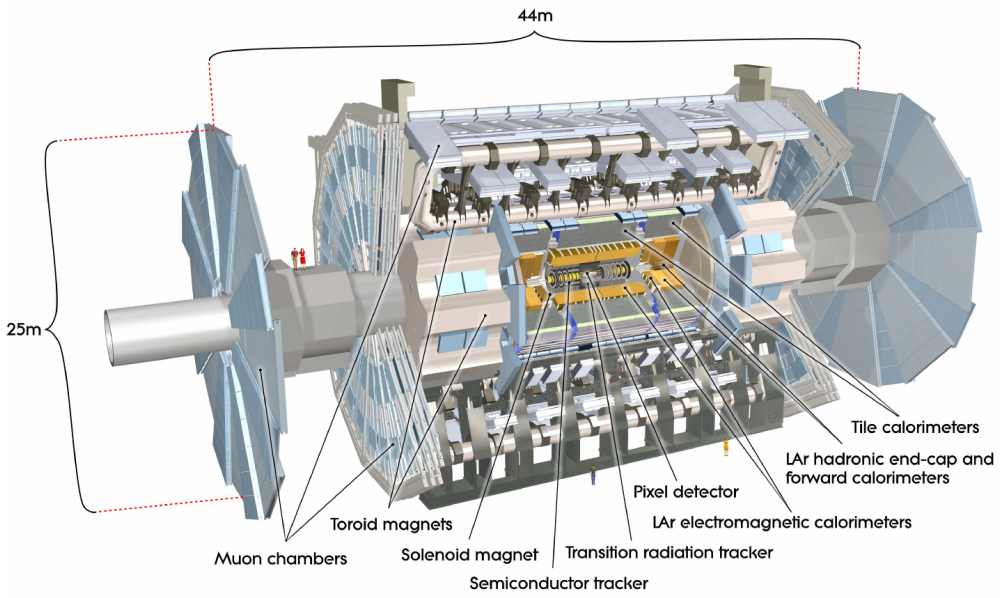

Figure 1.1: The general layout of the ATLAS detector[1].

covers the pseudorapidity range 1.5 to 4.9. The magnet configuration is as follows: the inner-detector cavity is surrounded by a thin superconducting solenoid and around the calorimeters are eight times three large superconducting toroids (that is always one in the barrel and two in the end-caps) arranged so that an eight-fold azimuthal symmetry around the calorimeters is achieved. In the Inner Detector (ID), a combination of discrete, high-resolution pixel and strip detectors in the inner part of the tracking volume, and straw-tube tracking detectors capable of generating and detecting transition radiation in the outer part, allows to achieve pattern recognition, momentum and vertex measurement and electron identification.

Energy and position resolution is provided by high granularity liquid-argon electromagnetic sampling calorimeters. The hadronic calorimetry is provided by a scintillator-tile calorimeter, segmented into a large barrel and two smaller extended barrel cylinders on both sides of the central barrel.

For the hadronic calorimetry is also used the liquid-argon technology matching the outer limits in pseudorapidity for the end-cap EM calorimeters. The liquid-argon forward calorimeters provide electromagnetic as well as hadronic energy measurements and extend the coverage in the high $|\eta|$ range.

Chapter 2

Overview of Quantum Chromodynamics

The main goal of this thesis is to measure the azimuthal correlation of the two jets with the highest transverse momenta p_T (leading and subleading jet). The jets originate from collisions of two protons at the Large Hadron Collider (LHC) with the centre of mass energy $\sqrt{s} = 13$ TeV. Due to the high energies, the fundamental theory that describes the dominant proton scatterings at the LHC is the Quantum Chromodynamics (QCD) or to be more precise its perturbative approach (pQCD). However it is impossible at the moment to describe proton-proton scattering using only basic QCD principles, the crux being the composite structure of the proton. A brief recapitulation of the classification of elementary particles and forces along with the proton structure is now presented as a prelude to the discussion of a few chosen properties of QCD such as the running coupling, colour confinement and asymptotic freedom.

Classification of elementary particles and fundamental interactions

Every elementary particle is a manifestation of its quantum field and can be viewed as its material fluctuation. Every particle can exist only within the boundaries of Heisenberg uncertainty principle. This means that even if the energy available in system is not sufficient to reach the mass of the particle, the particle can be said to exist withing a sufficiently small time window. Each particle is characterized by its mass, lifetime and a set of various quantum numbers for example intrinsic angular momentum (spin), electric charge and colour charge (charge of the strong interaction), parity, flavour and lepton number. The common classification is into quarks, leptons and intermediate bosons. A brief overview of their properties can be found in Fig. 2.1. It should be mentioned, that bosons are generally particles with integral spin and so

the particles in Fig. 2.1 are not the only bosons in existence. Quarks and leptons are included in the category called fermions, those are particles with half-integral spin that abide the Pauli exclusion principle.

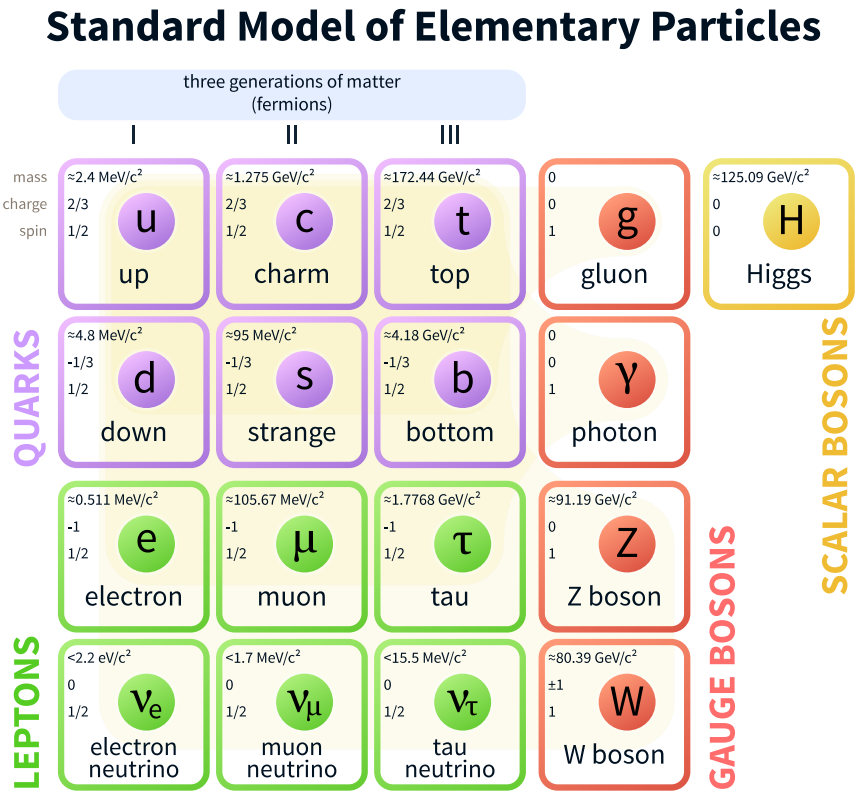

Figure 2.1: A table of quarks, leptons and intermediate bosons[2].

Quarks: As can be seen in Fig. 2.1 there are three generations of quarks with each generation more massive than the other. In each generation there are two quarks with different mass and charge. Each quark has its flavour, three colours and the charge of either $-\frac{1}{3}$ or $+\frac{2}{3}$ of elementary charge (e). This means that quarks are susceptible to all four interactions. Another interesting property of quarks is that they can never be found isolated and are ever in a bound into composite particles called hadrons. This property is more thoroughly discussed in the following chapter, along with other properties of quantum chromodynamics. Hadrons can be divided into mesons (bound states of a quark and an anti-quark, another example of bosons) and baryons (fermions that have three valence quarks).

Leptons: Those are the particles that do not participate in the strong interaction. They have the electric charge of either -1 e for electron, muon and tauon or 0 for their neutrinos.

Intermediate Bosons: The last category of particles shown in Fig. 2.1 is intermediate

bosons. The gauge bosons, are the quanta of strong (8 gluons), weak (W^+,W^- and Z^0) and electromagnetic (photon) field. The one scalar boson is the Higgs boson which is the boson that belongs to higgs field - the field that causes through interaction with all the other fields that their quanta gain their mass.

Fundamental interactions

The four forces above are all except for the gravitational described in terms of quantum field theory. And the theory that describes the behaviour of Electromagnetic, Weak and Strong interaction together is called the Standard Model (SM) of particle physics. The gravitational interaction is the weakest interaction and plays almost no role in particle physic (except for experiments like AeGiS or GBar that explore the effects of gravity on antimatter). Gravity is described using general relativity that is separate from SM and is omitted in this thesis.

Weak interaction

It is the weakest of the three interactions in SM with about $1.166 \cdot 10^{-5}$ the strength of the strong interaction at the m_Z scale [2]. Its quantum field formulation is called Quantum Flavour Dynamics (QFD), although this name is rarely used. It can affect every known particle but it has a finite range of about 10^{-18} m because of the high mass of its gauge bosons. The high mass is a consequence of spontaneous symmetry breaking caused by the Higgs mechanism. It is interesting that existence of the boson Z was discovered and explained first after unification of the electromagnetic and weak interaction into one Electoweak (EW) theory and the subsequent discovery of neutral currents in data measurement. Up until that point it was thought that there were only the charged bosons $W^{\pm}$ that are responsible for the β-decay of nuclei.

Electromagnetic interaction

It has the middle strength in the SM with about $\frac{1}{137.035}$ the strength of the strong interaction[2]. Its quantum field formulation is called Quantum Electrodynamics (QED). It can only influence particles that carry electric charge and it has infinite range due to the zero mass of photon. It is the best known interaction and is described by the Maxwell equations. It is the interaction that governs our day-to-day life because it binds electrons and nuclei into atoms and atoms into molecules and even light itself is an electromagnetic field.

Strong interaction

It is the strongest known interaction. Its quantum field formulation is called Quantum Chromodynamics (QCD). It influences only particles that carry colour charge(there are three colours and three anti-colours)but it has a finite range of about 10^{-15} m which is roughly the diameter of a proton. This of course does not mean that the interaction does not reach beyond this threshold and the remnant force that remains is the nuclear force that binds nuclei together in a loose analogy to the Van der Waals force, a remnant of EM interaction, that can bind atoms into molecules. A more thorough description of QCD is in the following chapter about the proton scattering and the properties of QCD

Standard model

The Standard Model of particle physics is the theory that binds together the three interactions above along with the Higgs mechanism into one compact theory. The Lagrangian of this theory is rather extensive and so it is not mentioned here because it plays only a background role in the context of this thesis as an underlying principle. The main theoretical idea behind its construction was that it should be invariant under the groups of symmetries SU(3)×SU(2)×SU(1) from which properties and/or existence of elementary particles arise. It describes how quarks and leptons come to be and how they acquire their mass through the Higgs mechanism. Another part is describing the electroweak interaction and the breaking of the SU(2) symmetry that causes gauge bosons of weak interaction to gain mass. Yet another part describes the existence of colour and why there are 8 gluons (this is caused by the fact that the Lagrangian is invariant under the group of SU(3)). The last part of the Lagrangian deals with the virtual particles. It is clear that the standard model is not perfect as evidenced by observations of neutrino oscillations that hint at the non-zero mass of neutrinos which is in contradiction with the SM condition that the neutrinos have similar to the photon zero mass. However this does not mean that SM is completely wrong because its predictions are in many experiments highly precise.

2.1 Proton structure

The first hints of proton being a composite particle came from the electron-proton scatterings at SLAC and DESY at beam energies between 1 and 20 GeV. Similar structure in electron-proton scatterings has been observed in the secondary electron spectra as in electron-nucleus scattering which was a clear sign of inner structure. These components of proton have later been identified as quarks. The cross section of elastic scattering of electron on proton that takes into account spin as well as magnetic

moment of proton, in dependence on the square of four-momentum transfer $Q^2 = -\mathbf{q}^2 = (\mathbf{k} - \mathbf{k}')^2$, has been derived by Rosenbluth and can be written as:

$$\left(\frac{d\sigma}{d\Theta}\right)_{Rsb} = \frac{2\alpha^2 E^2}{Q^4} \frac{\cos^2(\theta/2)}{1 + \frac{2E}{m_p}\sin^2(\theta/2)} \left[A(Q^2) + B(Q^2)\tan^2\frac{\theta}{2}\right], \tag{2.1}$$

where α is the fine structure constant, E is energy of the electron, Q^2 is the transfered momentum, θ is the scattering angle and m_p is the mass of the proton. $A(Q^2)$ and $B(Q^2)$ in Eq.(2.1) are formfactors:

$$A(Q^2) = \frac{G_E(Q^2) + \left(\frac{Q^2}{4m_p^2}\right) G_M(Q^2)}{1 + \frac{Q^2}{4m_p^2}},$$

$$B(Q^2) = \frac{Q^2 G_M(Q^2)}{2m_p^2}.$$

The dependence of both formfactors is in a good agreement with an experimentally determined dipole formula:

$$G(Q^2) = \frac{1}{\left(1 + \frac{Q^2}{m^2}\right)^2}. \tag{2.2}$$

The relation between both proton formfactors is quite simple: $G_E^p = \frac{G_m^p}{\mu_m^p}$ where μ_m^p is the anomalous magnetic moment of proton.

As values of Q^2 increase, the overall importance of elastic scattering decreases and inelastic scattering rises into prominence. Let us consider the process $ep \to eX$ where X is a hadron system with the invariant mass W. The square of invariant mass in laboratory frame is $W^2 = (\mathbf{p} + \mathbf{q})^2 = 2m_p\nu + m_p^2 + q^2$, where ν is the transfered energy and $\mathbf{p} = (m_p, 0, 0, 0)$ is the four momentum of proton in laboratory frame. Therefore

$$Q^2 = 2m_p\nu = m_p^2 - W^2. \tag{2.3}$$

In the case of inelastic scattering, W^2 can differ from m_p^2 which means that Q^2 and ν are independent variables. The differential cross section of inelastic $e-p$ scattering in laboratory frame can be written in similar form as Eq.(2.1):

$$\frac{d^2\sigma}{d\Omega dE'} = \frac{4\pi\alpha^2 E'^2}{Q^4} \left[W_2(Q^2,\nu)\cos^2\frac{\theta}{2} + 2W_1(Q^2,\nu)\sin^2\frac{\theta}{2}\right], \tag{2.4}$$

where $W_1(Q^2,\nu)$ and $W_2(Q^2,\nu)$ are the so called structure functions of proton which replace the elastic fromfactors G_E and G_M. Inelastic processes are best described by the momentum transfer Q^2 and the Bjorken variable $x = \frac{Q^2}{2\mathbf{pq}}$ where $x = 1$ holds for the elastic scattering and for the inelastic is always < 1 because $W^2 > m_p^2$. For low x and high Q^2, is the region of the Deep Inelastic Scattering (DIS). The meaning of DIS is that the inner structure of proton comes into play. In 1969, Richard Feynman has

proposed a hypothesis that DIS cross section of electron on proton can be expressed as a composite spectrum of elastic scatterings of electron on partons, that carry only a portion of the whole momentum of the whole proton, this portion being expressed by the Bjorken x[17]. Assuming that partons are spin 1/2 particles, we can express the cross section for scattering of the electron on i-th parton as:

$$\frac{d^2\sigma^i}{d\Omega dE'} = \frac{4\pi\alpha^2 E'^2}{Q^4}\left[e_i^2\cos^2\frac{\theta}{2} + e_i^2\frac{Q^2}{2m_i^2}\sin^2\frac{\theta}{2}\right]\delta(\nu - \frac{Q^2}{2m_i}), \tag{2.5}$$

where e_i is the charge of parton expressed in units of positron charge. As every parton carries different part of the momentum x, it is necessary to multiply the cross section (2.5) by a weighting function $f_i(x)$ that defines the probability that parton i carries fraction of momentum x before adding it into the composite DIS cross section. Assuming that the electron-parton scattering leaves the state of other partons unchanged, the whole cross section of electron proton can be expressed as following sum:

$$\frac{d^2\sigma}{d\Omega dE'} = \sum_i \int_0^1 \frac{d^2\sigma^i}{d\Omega dE'} f_i(x)dx. \tag{2.6}$$

A new form of expression of the structure functions W_1 and W_2 can be obtained by comparing (2.4) and (2.6):

$$m_p W_1(\nu, Q^2) \equiv F_1(x) = \sum_i \frac{e_i^2}{2} f_i(x), \tag{2.7}$$

$$\nu W_2(\nu, Q^2) \equiv F_2(x) = \sum_i e_i^2 x f_i(x). \tag{2.8}$$

It is rather obvious that the new structure functions F_1 and F_2 depend exclusively on x, this property is known as a Bjorken scaling. Their relationship is summarised into the Callan-Gross relation:

$$2xF_1(x) = F_2(x) \tag{2.9}$$

that holds only if the spin of parton is 1/2, which has been experimentally confirmed in the SLAC laboratory[18]. This exclusive dependence on Bjorken x holds for $x \gtrsim 0.05$ as is demonstrated in Fig.S2.2. This is discussed below after the introduction of running coupling.

This experimental proof has been one of the reasons that partons have been identified as quarks. Those have been successfully used for explaining many static hadron properties. Quantum numbers of a proton can be explained using the assumption that the proton consists of two up(u) a one down(d) quarks. These are called the valence quarks. The same numbers can be obtained if proton contains any number of additional quark-antiquark pairs, because their additive quantum numbers are equal to zero. Those are called the sea quarks. Let $f_i(x)$ denote the parton distribution function

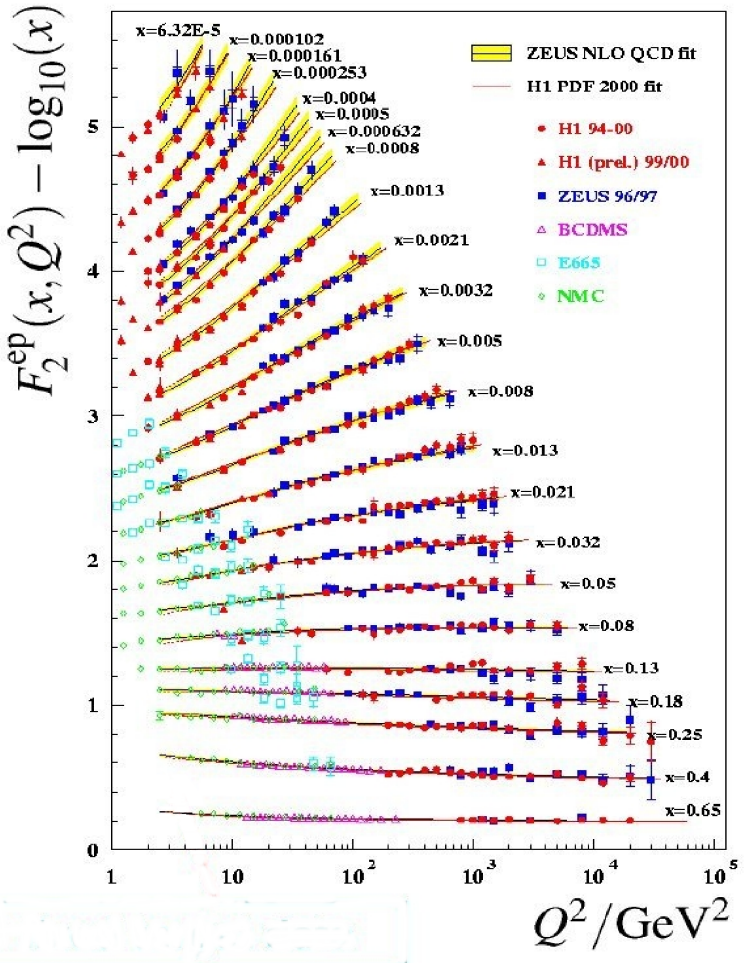

Figure 2.2: The dependence of structure function $F_2(x, Q^2)$ on the momentum transfer Q^2.

(PDF) of the parton i in a nucleon. It is possible to express any PDF in the form of a distribution function for valence and sea quarks:

$$f_i(x) \;=\; V_i(x) \;+\; S_i(x). \tag{2.10}$$

If the only flavours that are taken into account are up, down and strange, the structure functions of proton and neutron can rewritten as:

$$\begin{aligned} F_2^{ep} &= \frac{x}{9}[4V_u(x) \;+\; V_d(x)] \;+\; \frac{4}{3}xS(x), \\ F_2^{en} &= \frac{x}{9}[V_u(x) \;+\; 4V_d(x)] \;+\; \frac{4}{3}xS(x), \end{aligned}$$

where V_i are the valence quark PDFs and S is the sea quarks PDF (assuming that all see quarks have the same distribution). The V_s and those of antiquarks have been omitted due to them being equal to zero as expected.

Considering scattering of a proton on a nucleus with equal number of protons and neutrons, an average structure function of a nucleon N can be expressed as:

$$F_2^{eN} = \frac{1}{2}(F_2^{ep} + F_2^{en}), \tag{2.11}$$

$$F_2^{eN} = x\left[\frac{5}{18}[f_u(x) + \overline{f}_u(x) + f_d(x) + \overline{f}_d(x)] + \frac{1}{9}[f_s(x) + \overline{f}_s(x)]\right], \tag{2.12}$$

It would be reasonable to expect, that the summed momentum of partons should be equal to the momentum of the proton, i.e.:

$$\int_0^1 x[f_u(x) + \overline{f}_u(x) + f_d(x) + \overline{f}_d(x) + f_s(x) + \overline{f}_s(x)]dx = 1.$$

Therefore it could be assumed that, approximating the influence of strange quarks as negligible:

$$\frac{18}{5}\int_0^1 F_2^{eN}dx \simeq 1.$$

However the experimental value derived from cross sections of charged leptons on carbon nucleus is around 0.5, which means that quarks and antiquarks share only about half of the whole momentum of a nucleon. The rest of the momentum is carried away by other components that are inside the nucleon, but are invisible to the electromagnetic and weak force. These components are called gluons and have no electric or weak charge, but they do have colour charge. The direct consequence of gluons carrying colour charge is that they are capable of self-interaction (see Fig. 2.3) this property and its other consequences are discussed in the following section. The distribution of momentum carried by gluons is characterised by the gluon distribution function, usually denoted $g(x)$.

Figure 2.3: Lowest order feynman diagrams depicting the self-interactions of gluons.

2.2 Quantum Chromodynamics

Now it is time to introduce the QCD in a greater detail. QCD is a non-abelian gauge theory which is based on the $SU(3)$ colour gauge group due to the fact that QCD has

to comply to several experimental and theoretical conditions such as the existence of $q\overline{q}$(mesons), qqq(baryons) and potential tetra- or penta-quark bound states, asymptotic freedom of quarks and long range cut-off of the strong interaction. From the existence of bound states such as Δ^{++} which has three identical quarks, the need for three different colour states(red, green and blue) can be derived. To this day, the existence of tetra- and penta-quarks is the subject of intense studies for example at the LHCb experiment such as [19] for tetra-quarks and [20] for penta-quarks. Expecting the particle/antiparticle symmetry one arrives to:

$$3 \otimes 3 = 1 \oplus 8 \tag{2.13}$$

which gives the colour octet of gauge bosons = gluons that supply the colour interaction and one colour singlet that does not. The colour octet states of gluons are:

$$\frac{1}{\sqrt{2}}(r\overline{b} + b\overline{r}) \qquad \frac{-i}{\sqrt{2}}(r\overline{b} - b\overline{r})$$

$$\frac{1}{\sqrt{2}}(r\overline{g} + g\overline{r}) \qquad \frac{-i}{\sqrt{2}}(r\overline{g} - g\overline{r})$$

$$\frac{1}{\sqrt{2}}(b\overline{g} + g\overline{b}) \qquad \frac{-i}{\sqrt{2}}(b\overline{g} - g\overline{b})$$

$$\frac{1}{\sqrt{2}}(r\overline{r} - b\overline{b}) \quad \frac{-i}{\sqrt{6}}(r\overline{r} + b\overline{b} - 2\,g\overline{g})$$

and the colour singlet state is:

$$\frac{1}{\sqrt{3}}(r\overline{r} + b\overline{b} + g\overline{g}).$$

The Lagrangian of QCD has a standard form [21]:

$$\mathscr{L}_{QCD} = \overline{\psi}(i\gamma^{\mu}\mathscr{D}_{\mu} - m)\psi - \frac{1}{2}\mathrm{Tr}(G_{\mu\nu}G^{\mu\nu}), \tag{2.14}$$

where ψ is the spinor colour triplet of quarks

$$\psi = \begin{pmatrix} q_r \\ q_b \\ q_g \end{pmatrix}, \tag{2.15}$$

and $\mathscr{D}_{\mu}$ is the covariant derivative :

$$\mathscr{D}_{\mu} = \partial_{\mu} + igB_{\mu} \tag{2.16}$$

where B_{μ} is a 3x3 matrix in colour space composed from colour gauge fields b^{l}_{μ} and the generators of the $SU(3)$ group $\lambda^{l}/2$:

$$B_{\mu} = \frac{1}{2}\lambda^{l}b^{l}_{\mu}. \tag{2.17}$$

The $G_{\mu\nu}$ in (2.14) is the gluon field-strength tensor:

$$G_{\mu\nu} = (ig)^{-1}[\mathscr{D}, \mathscr{D}] = \partial_\nu B_\mu - \partial_\mu B_\nu + ig[B_\nu, B_\mu].$$

A more in-depth discussion of properties of the λ matrices, along with more rigorous derivation of QCD as group theory can be found for example in [21]. The following paragraphs focus more on a few crucial aspects and properties of QCD and its' perturbative variant.

2.2.1 Running coupling

One of the key things about QCD is the value of its coupling constant which can serve as an expression of the relative strength of QCD in comparison with the other interactions. The definition of coupling constant of the strong interaction is standard:

$$\alpha_S = \frac{g^2}{4\pi}, \tag{2.18}$$

where g is the dimensionless coupling constant from the definiton of covariant derivation (2.16) and gluon strength tensor $G_{\mu\nu}$.

The value of α_S is important mainly in perturbative QCD (pQCD) where observables are usually expressed in terms of the renormalized coupling. Contrary to what its name suggests, α_S is not a constant, but has dependency on the (non-physical) renormalization scale μ_R^2. In order to compare the strength of QCD, the value of renormalization scale must be close to the value of momentum transfer: $\alpha_S(\mu_R^2 \simeq Q^2)$. The behaviour of the value of α_S in relation to Q^2 is called the running coupling and is governed by the renormalization group equation[2]:

$$\mu_R^2 \frac{d\alpha_S}{d\mu_R^2} = \beta(\alpha_S) = -(c_0\alpha_S^2 + c_1\alpha_S^3 + \ldots), \tag{2.19}$$

$$c_0 = \frac{33 - 2n_f}{12\pi} \tag{2.20}$$

$$c_1 = \frac{153 - 12n_f}{24\pi^2} \tag{2.21}$$

where the c_k are the $(k+1)$-loop β-function coefficients, n_f is the number of quark flavours considered light ($m_q \ll \mu_R$). The precise value of loop coefficients c_k depends on the renormalization scheme with the value given here coming from the most widely used modified minimal subtraction scheme ($\overline{MS}$). If all, but c_0 loop coefficients are neglected and the number of flavours is taken as a constant, then the exact analytic solution for equation (2.19) is

$$\alpha_S(\mu_R^2) = \frac{1}{c_0 \ln\left(\frac{\mu_R^2}{\Lambda^2}\right)}. \tag{2.22}$$

The Λ is a constant of integration which denotes the scale where the perturbative coupling would diverge. Its value indicates the energy range where non-perturbative effects dominate. Because the exact value of Λ that defines the value of α_S is scheme and n_f dependent, the standard practice for quoting the value of α_S is to state the value at a given scale, typically mass of Z boson M_Z instead of at the value of Λ.

An example of the running coupling can be seen in the Fig. 2.4 along with the comparison of shift of the curve that is caused by using a different renormalization scheme.

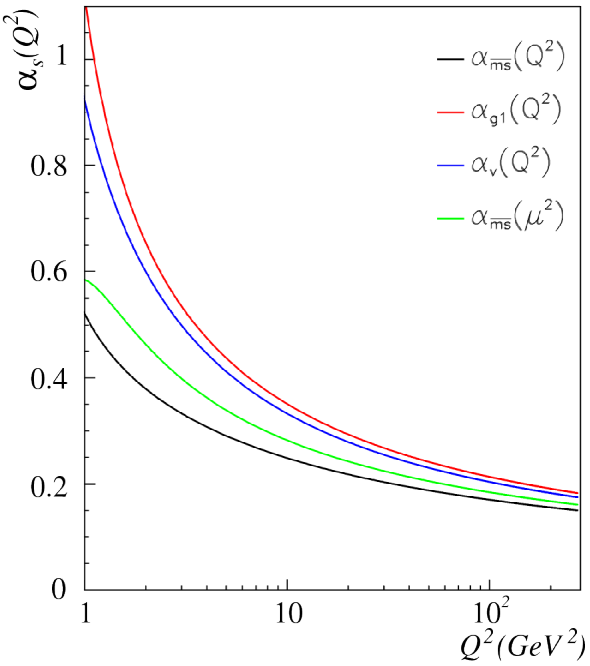

Figure 2.4: The demonstration of the effect of different renormalization schemes on the running coupling of QCD[3].

More detailed discussion of the effects of different renormalization schemes and n_f values on the running coupling can be found in [3].

As was demonstrated in Fig. 2.2, the constant behaviour of structure function breaks down for small values of Bjorken x. This behaviour can be explained using renormalization procedures which yield the Dokshitzer-Gribov-Lipatov-Altarelli-Parisi(DGLAP) parton evolution equations (2.23) and (2.24) for redefining the quark an gluon PDFs into their renormalized forms where the factorization scale μ_F is introduced to ensure the logarithmic scaling.

$$\frac{\partial f_i(x,\mu_F^2)}{\partial \log \mu_F^2} = \frac{\alpha_S}{2\pi}\int_x^1 \frac{dz}{z}\left[P_{q_iq_j}(z,\alpha_S)f_j(\frac{x}{z},\mu_F^2) + P_{q_ig}(z,\alpha_S)g(\frac{x}{z},\mu_F^2)\right], \tag{2.23}$$

$$\frac{\partial g(x,\mu_F^2)}{\partial \log \mu_F^2} = \frac{\alpha_S}{2\pi}\int_x^1 \frac{dz}{z}\left[P_{gq_j}(z,\alpha_S)q_j(\frac{x}{z},\mu_F^2) + P_{gg}(z,\alpha_S)g(\frac{x}{z},\mu_F^2)\right], \tag{2.24}$$

The $P_{ab}(z, \alpha_S)$ are splitting functions, where first index denotes the final state particle that carries the momentum fraction z and the second index is the initial particle that undergoes splitting. Usually the factorization scale μ_F is taken to be identical to the renormalisation scale μ_R.

2.2.2 Colour confinement and asymptotic freedom

One of the interesting properties of quantum chromodynamics is the phenomenon of asymptotic freedom. That is if a colour charge is inspected under small space scales, in other words in processes with high momentum transfers, the value of strong coupling is falling precipitously as can be seen in Fig. 2.4. As a result of this low value of α_S, the relative strength of force that is affecting a colour charge is falling and the charge behaves almost freely. Other interpretation can be that the effective colour charge of the object is distorted by creation of pairs of colourful objects such as quark and gluon loops as is demonstrated in Fig.2.5.

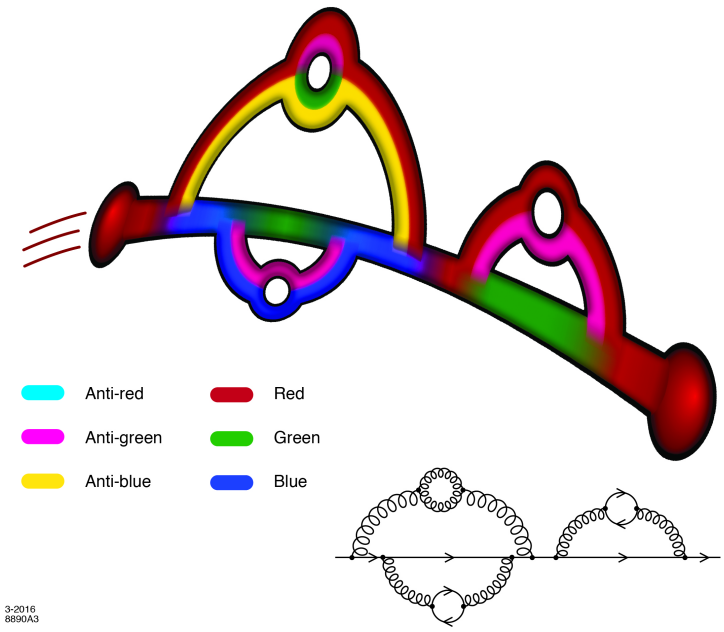

Figure 2.5: Demonstration of colour charge antiscreening via the creation of quark and gluon loops. [3]

On the other hand, α_S rises as a logarithm at larger distances/smaller momentum transfers. However due to the fact, that proton has a finite size this growth cannot be indefinite. This means that the colour charge has to be confined. That in turn implies existence of a certain cutoff for the value of α_S. The specific value of this cutoff is the subject of phenomenological studies.

Chapter 3

Compilation of previous measurements

The study of dijet azimuthal correlation (sometimes called decorrelation) is an important tool of testing the properties of the Standard Model of particle physics and pQCD. One of the properties of QCD that can be tested through azimuthal correlation measurements is the running coupling of the strong interaction mentioned in previous chapter. The α_S can be measured through different techniques for example from p_T and E_T spectra or ratios of jet multiplicities. This chapter is aimed to provide a brief overview of available research starting from standard control plots that will be used for consistency checking of our analysis, followed by a brief foray into measurement techniques of dijet azimuthal correlation and closing with an overview of α_S measurements using different approaches.

3.1 Measurement of control variables

It is a good practice to have a few control variables that are measured along with every new observable in order to ensure the basic consistency of our measurement with the rest of the scientific field. As this point of reference have been chosen the double-differential cross-sections for inclusive jets and dijets. More specifically the inclusive jet cross-section is taken as a function of rapidity y and transverse momentum p_T. The inclusive jet double-differential cross section is expressed as the ratio:

$$\frac{d^2\sigma}{\mathrm{d}p_T\mathrm{d}y} = \frac{N_{\text{jets}}}{\mathcal{L}\Delta p_T \Delta y}, \tag{3.1}$$

where N_{jets} is the number of jets in the data sample after correcting for detector effects, $\mathcal{L}$ is the integrated luminosity of the data sample given in the bins of transverse momentum Δp_T and rapidity Δy. The dijet cross-section is taken to be a function of half the rapidity separation of the two leading jets:

$$y^* = \frac{1}{2}|y_1 - y_2|, \tag{3.2}$$

and the mass of the dijet system m_{jj}. The y^* dependency is chosen because y^* is invariant under a Lorentz boost along the z-direction and is equal to the absolute rapidity of each jet in the dijet rest frame. The dijet double-differential cross section is expressed as the ratio:

$$\frac{\mathrm{d}^2\sigma}{\mathrm{d}m_{jj}\mathrm{d}y^*} = \frac{N_{\mathrm{jets}}}{\mathcal{L}\Delta m_{jj}\Delta y^*}, \tag{3.3}$$

The measurements that are considered here have been carried out by the ATLAS and CMS collaborations for example in the studies [4] and [22] respectively. More studies are mentioned below in the section about measurement of α_S from transverse momentum and transverse energy spectra.

3.1.1 ATLAS 13 TeV measurement

The study [4] measures the inclusive jet and dijet cross-sections in proton-proton collisions at the centre-of-mass energy of 13 TeV. The data have been collected in 2015 by the ATLAS detector at the LHC. The integrated luminosity of the data sample is 3.2 fb^{-1}. The studied jets are reconstructed using the anti-k_t jet algorithm with the radius parameter $R = 0.4$. The kinematic range of the measurement is defined for double-differential inclusive jet and for double-differential dijet production. The former is measured as a function of transverse momentum p_T in the range of $p_T \in (100, 3500)$ GeV, and absolute rapidity up to $|y|= 3$. The latter is measured as a function of the mass of the dijet system $m_{jj} \in (300, 9000)$ GeV, and the half of absolute rapidity separation y^* between the two jets with the highest p_T(leading jets) within $|y|< 3$. The constraint on y^* is $y^* \leq 3$. Additional demands on dijet phase space is that the two leading jets have $p_T > 75$ GeV and that the scalar sum of their transverse momenta is higher than 200 GeV.

The measured data are compared with simulated jet events produced by Monte Carlo (MC) generators. Pythia 8 was used to establish a baseline for comparisons. The basic matrix element was LO pQCD for the process $2 \to 2$, along with leading-logarithmic(LL) p_T-ordered parton shower and hadronisations with Lund string model. The MC samples were created using the set of LO Parton Distribution Functions NNPDF2.3LO, with parameters tuned according to the A14 tune [23]. The NLO samples were produced using Powheg matrix elements and Pythia 8 for showering. In the NLO case was used the PDF set CT10 again with the A14 tune.

Results

The results of double-differential inclusive jet cross section measurement are shown in Fig. 3.1. The cross section is depicted as a function of p_T in six rapidity bins. The p_T range covered by the inclusive jet measurement is from 100 GeV to 3.5 TeV.

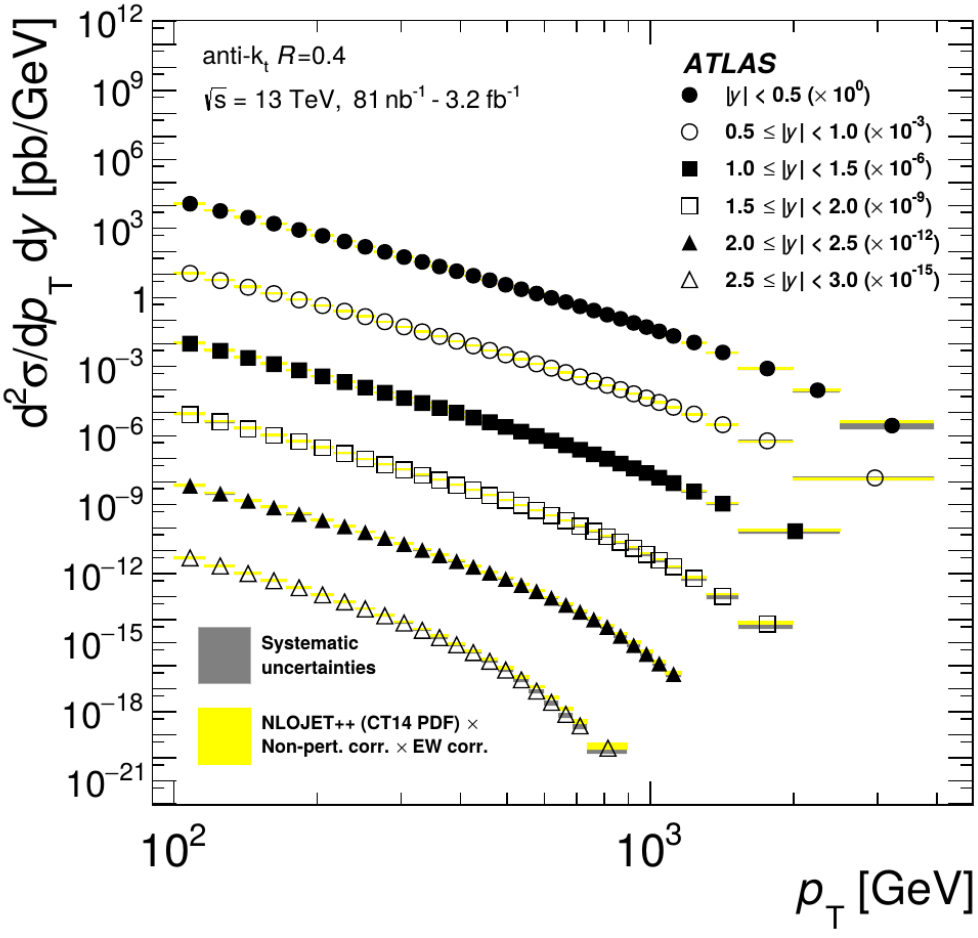

Figure 3.1: The doubly-differential cross section of inclusive jet production as a function of transverse momentum in six bins of absolute rapidity [4].

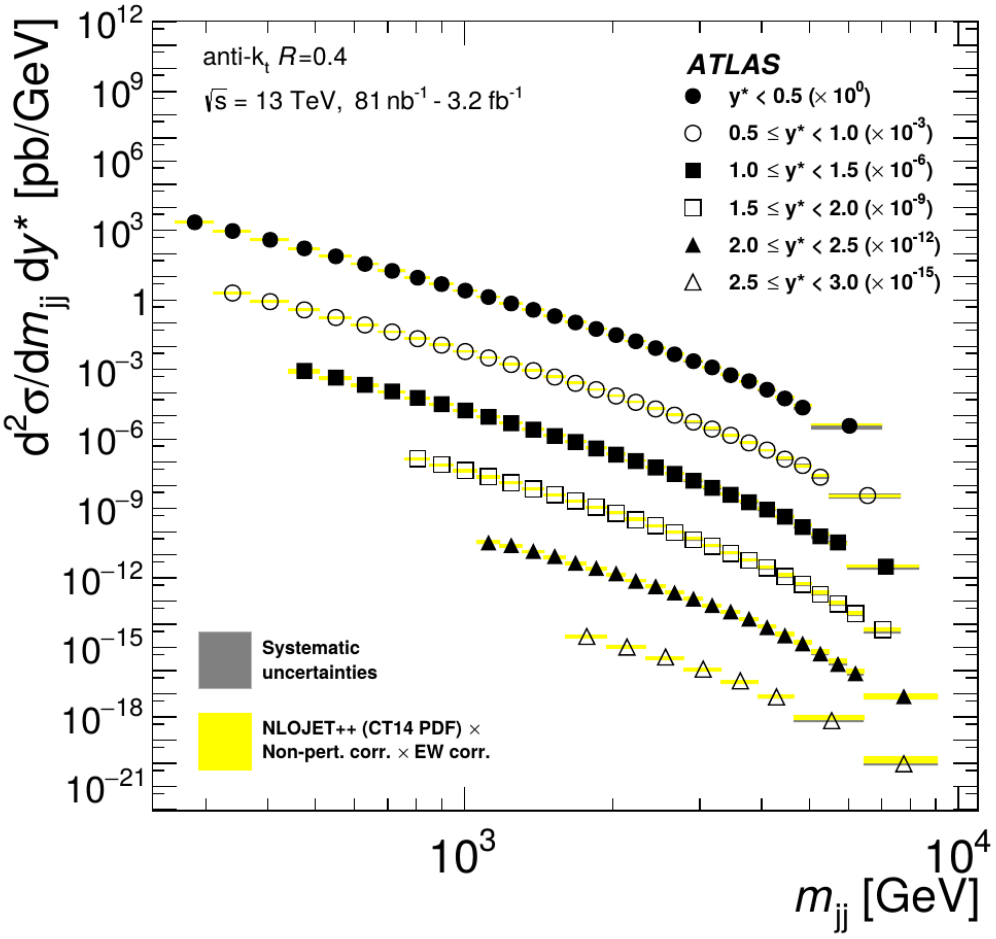

Figure 3.2: The doubly-differential cross section of dijet production as a function of the mass of dijet system in six bins half the absolute rapidity separation of the two leading jets [4].

The results of double-differential dijet cross section measurement are shown in Fig.3.2. The cross section is shown as a function of the mass of the dijet system m_{jj} in six bins of y^*. The m_{jj} range of the measurement is from 300 GeV to 9 TeV for $y^* < 3$.

Similar studies of inclusive jet and dijet cross sections are done regularly at every experiment at the LHC. As an example we can mention the CMS experiment and their study [22] that measures the differential cross section of dijet production as a function of dijet mass.

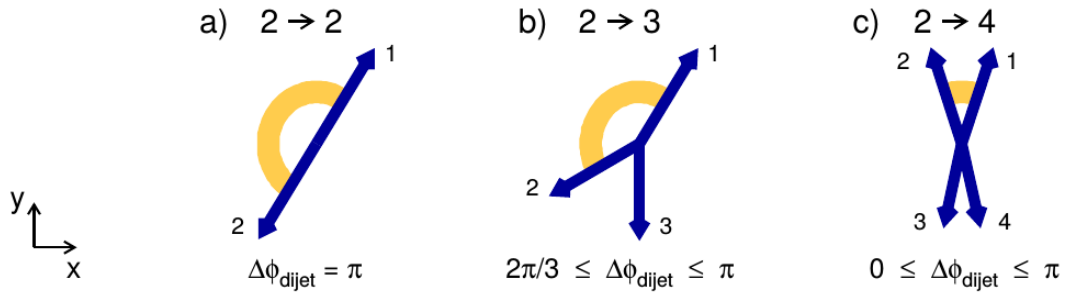

Figure 3.3: Demonstration of the meaning of $\Delta\phi$ [5].

3.2 Measurement of azimuthal correlation

Let us now present an overview of previous measurements of leading dijets azimuthal correlation, or dijet decorrelation as it is called in some studies. Throughout the years, azimuthal correlation of particle showers have been studied by various experiments on hadron colliders such as the D0, CMS or ATLAS. Because in the next chapter, that concerns data analysis, the analyzed data were measured by the ATLAS experiment, the primary focus of this section is on the ATLAS measurements and the rest of the experiments is presented only to provide a broader insight into the evolution of azimuthal correlation measurements. The most common definition of azimuthal correlation, that is used in this thesis as well is for events, that contain at least two particle jets. It is taken to be the absolute value of separation in azimuthal angle between the two leading jets:

$$\Delta\phi = |\phi_{leading} - \phi_{subleading}|. \tag{3.4}$$

The main advantage of $\Delta\phi$ is that it is a clean and simple way to study radiative processes in QCD. The Fig.3.3 demonstrates the meaning of jet azimuthal correlation.

Dijet production in hadron collisions without additional radiative effects results in two jets with equal transverse momenta and correlated azimuthal angles $\Delta\phi = \pi$. Soft radiation causes only a small deviation from this value. However, $\Delta\phi$ significantly lower than π is an evidence of additional hard radiation with high p_T simply because of the four-momentum conservation. Exclusive 3-jet production is concentrated in the region $\Delta\phi \in (\frac{2\pi}{3}, \pi)$, while smaller smaller $\Delta\phi$ indicates events with jet multiplicity four or higher. The main advantage of $\Delta\phi$ is the possibility to test higher order pQCD predictions without requiring the reconstruction of additional jets (which was especially useful historically, when computational resources and measurement precision were limited) and providing a possible way to examine the transition between soft and hard QCD processes based on a single observable. Another possible uses for

azimuthal correlation are search for new physical phenomena with dijet signatures such as supersymmetric extensions of the Standard Model or the testing of the value of strong coupling, which is discussed below.

D0 Collaboration

One of the earlier studies of azimuthal correlation was from D0 experiment at the Tevatron proton-antiproton collider [6]. The collisions had centre-of-mass energy of 1.96 TeV and the integrated luminosity of the data sample used in analysis was 150 pb^{-1}. The measured jets were reconstructed using an iterative seed-based cone algorithm (including mid-points) with radius $R = 0.7$. For more information on jet algorithm see i.e.[24]. The azimuthal correlation was measured in four p_T ranges: $p_T > 75$, 100, 130 GeV for the leading jet and the second leading jet was required to have $p_T > 40$ GeV. Additionally, both jets were required to be in central rapidity region of $|y| < 0.5$. The measured distributions along with LO MC predictions from Herwig 6.505 and Pythia 6.225 (both using default parameter and the PDF set CTEQ6L) can be found in Fig. 3.4. It is plain to see, that in this instance Herwig describes the data accurately over the whole range, whereas Pythia with default settings(blue dashed line) tends to undervalue the data points in the lower region and peaks too sharply at $\Delta\phi = \pi$. The discrepancy between Pythia and data can be rectified (blue bands in Fig.3.4) if one allows tuning of maximum virtuality which influences the initial state parton shower. Nevertheless, the biggest disparity between Pythia and Data is in the low-$\Delta\phi$ region, that would be dominated mainly by 3 and 4 jet production, and therefore the LO 2 to 2 model that is employed by Pythia cannot be realistically expected to describe the data flawlessly.

CMS Collaboration

Another study of azimuthal correlation was undertaken by the CMS collaboration in 2011 [7]. The study used data from proton-proton collisions at centre-of-mass energy of 7 TeV. The integrated luminosity of the inclusive dijet event sample was 2.9 pb^{-1}. Jets were reconstructed using the anti-k_T algorithm with the radius parameter $R = 0.5$. Events were selected if the two leading jets had $p_T > 30$ GeV and $|y| < 1.1$. Measurements were divided into five exclusive regions in p_T^{max} : (80, 110) GeV, (110, 140) GeV, (140, 200) GeV, (200, 300) GeV and above 300 GeV. Theoretical predictions were made using the MC generators Pythia 6, Pythia 8.135, Herwig++ and MadGraph 4.4.32 showered by Pythia 6. All versions of Pyhia and MadGraph used the CTEQ6L PDF set and Herwig uses the MRST2001 PDF set. The study focused on normalized distributions in order to better emphasize the shape of the spectrum. The results can be found in Fig. 3.5. Pythia6 and Herwig describe the shape of the data distributions

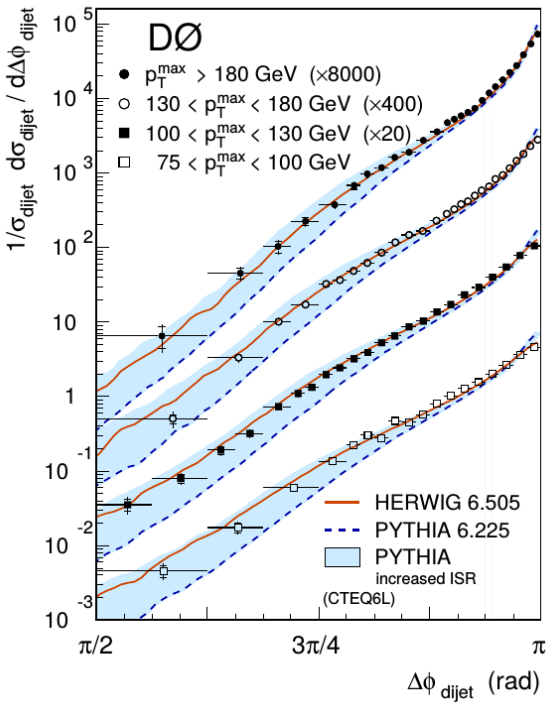

Figure 3.4: The distributions of $\Delta\phi$ in different p_T ranges. Black markers denote measured data, blue line and band denote Pythia 6.225 and red line denote Herwig 6.505 [6].

well, while MadGraph tends to underestimate them and Pythia8 tends to overestimate them.

ATLAS

The study [8] is a take on measurement of azimuthal correlation by the ATLAS collaboration. It is based upon 36 pb^{-1} of data from proton-proton collisions at the LHC as measured by the ATLAS detector at the centre-of-mass energy of 7 TeV. The measured jets are reconstructed using the anti-k_t algorithm with radius $R = 0.6$. In order to be considered, the jets are required to have $p_T > 100$ GeV and $|y| < 2.8$. Additionally, the two leading jets, that define the $\Delta\phi$ have to satisfy $|y| < 0.8$. By this choice, the measurement is restricted to a central y region where momentum fractions of the interacting partons are roughly equal and the experimental acceptance for multijet production is increased. The measurement is divided into 9 exclusive p_T ranges and its' results can be found in Fig. 3.6 overlaid with results from NLO pQCD calculation from NLOJET++ with fastNLO using the MSTW 2008 PDF.

The measured data are compared with MC simulations from SHERPA (which matches higher order tree-level pQCD diagrams with dipole parton shower), Pythia and Herwig (which uses LO 2 to 2 pQCD matrix elements matched with phenomeno-

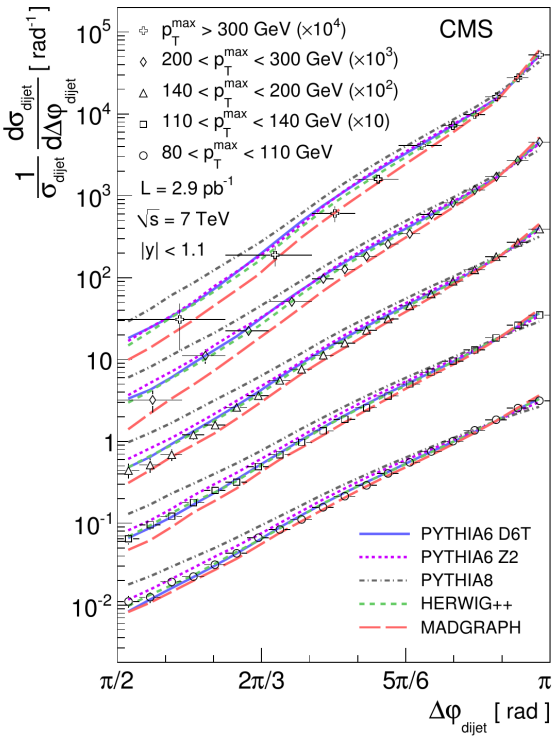

Figure 3.5: Normalized azimuthal correlation distribution in several p_T^{max} ranges. Lines represent MC predictions from Pythia6, Pythia8 Herwig++ and MadGraph+Pythia [7].

logical parton cascade showers) as well, however the results are not shown here but can be found in [8] Fig. 4.

3.3 Measurements of strong coupling

3.3.1 Transverse momentum and energy spectra

A few of the basic properties that can be measured and then used to determine the value of α_S are the transverse momentum spectrum and energy spectrum of inclusive jet measurements. The value of α_S is usually determined from sets of these inclusive jet cross section data points and then through minimizing the χ^2 function between data and the theoretical value, with α_S as a free parameter.

D0 Collaboration

One of the first measurements of strong coupling constant α_S was carried out by the D0 Collaboration [9]. Its value was determined from the energy dependence and transverse momentum dependence of the inclusive jet cross section in $p\bar{p}$ collisions at the Fermilabs Tevatron Collider with $\sqrt{s} = 1.96$ TeV. The strong coupling constant was determined

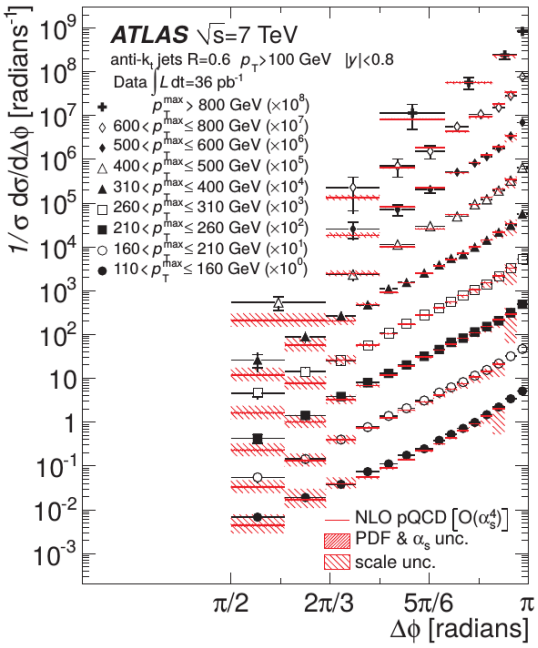

Figure 3.6: The normalized differential cross section binned in nine p_T^{max} regions (black markers). Compared with NLO pQCD calculations (red line). The hatched regions signify the theoretical uncertainties [8].

in a transverse momentum range $p_T \in (50,\ 145)$ GeV. The jets were reconstructed using iterative midpoint cone algorithm with cone radius of 0.7 in rapidity and azimuthal angle.

The results obtained by D0 were based on 22 selected data points, which have been grouped to produce the 9 data points that can be seen in Fig. 3.7. The figure shows a comparison to results from HERA DIS jet data and a Renormalisation Group Equation prediction for the combined D0 fit result and its uncertainty.

The value of $\alpha_S(M_Z)$ have been determined as:

$$\alpha_S(M_Z) = 0.1178^{+0.0081}_{-0.0095}(\text{exp.})^{+0.0071}_{-0.0047}(\text{scale}) \pm 0.0059(\text{PDF}) \tag{3.5}$$

ATLAS

The study [10] by the ATLAS collaboration at the LHC in CERN evaluates the strong coupling constant using the Transverse Energy to Energy Correlation(TEEC) and its Asymmetry (ATEEC). These quantities have been chosen, because jet energy alone is not Lorenz invariant under longitudinal boost along the beam direction and so the use of transverse energy $E_T = E\sin(\theta)$ makes more sense. Furthermore, according to study [25], the NLO corrections of TEEC and ATEEC are of moderate size, because at NLO they depend quadratically on the value of α_S, and therefore are well suited for

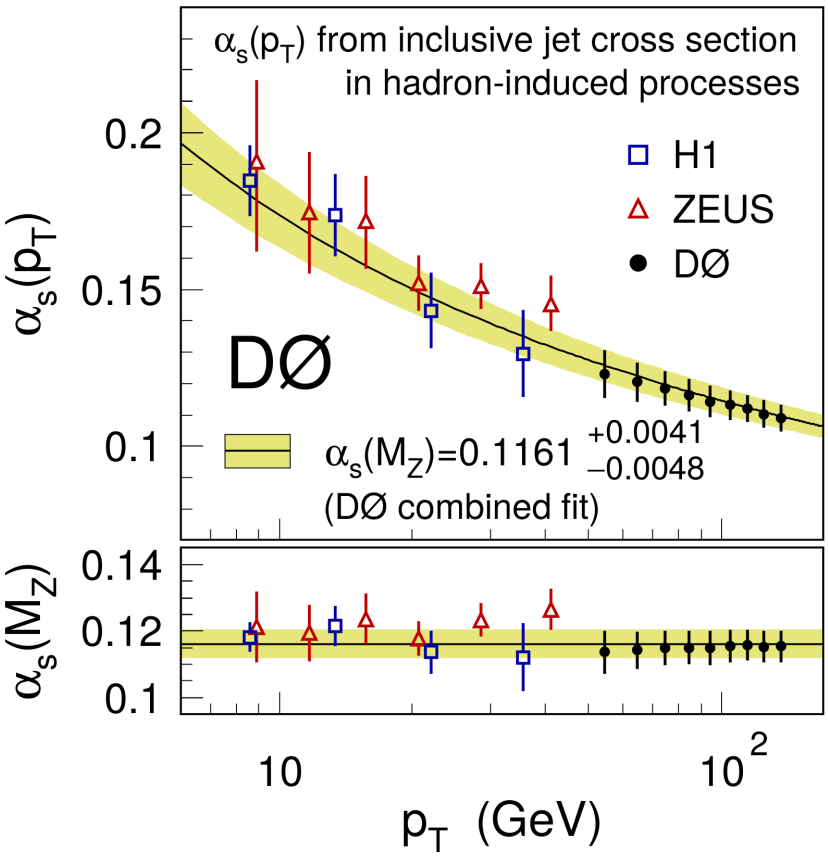

Figure 3.7: The dependency of α_S on transverse momentum (top) and the results of $\alpha_S(M_Z)$(bottom) [9].

its precision determination. The definitions of TEEC and ATEEC are [10]:

$$\frac{1}{\sigma}\frac{\mathrm{d}\Sigma}{\mathrm{d}\cos\phi} = \frac{1}{N}\sum_{A=1}^{N}\sum_{ij}\frac{E_{Ti}^{A}E_{Tj}^{A}}{\left(\sum_k E_{Tk}^{A}\right)^2}\delta\left(\cos\phi - \cos\phi_{ij}\right), \tag{3.6}$$

$$\frac{1}{\sigma}\frac{\mathrm{d}\Sigma^{\mathrm{asym}}}{\mathrm{d}\cos\phi} = \frac{1}{\sigma}\frac{\mathrm{d}\Sigma(\phi)}{\mathrm{d}\cos\phi} - \frac{1}{\sigma}\frac{\mathrm{d}\Sigma(\pi-\phi)}{\mathrm{d}\cos\phi}, \tag{3.7}$$

where N is the number of events in data sample, A is the event index, i and j are jet indexes, E_{Ti}^{A} is the transverse energy of i-th jet, ϕ_{ij} is the azimuthal angle between the jets, and the δ-function ensures that $\phi = \phi_{ij}$. The data used were recorded by the ATLAS detector at the LHC in 2012 in proton-proton collisions with $\sqrt{s} = 8$ TeV. The data were taken using a single-jet trigger that requires at least one jet, reconstructed with the anti-k_t algorithm with radius parameter R =0.4. The transverse energy in the trigger system is required to be greater than 360 GeV at the trigger level. In order to be fully efficient, the trigger demands that the scalar sum of p_T for the two leading jets(H_{T2}) is above 730 GeV. The integrated luminosity of the full data sample for this lowest unprescaled trigger is 20.2fb^{-1}. Selected jets must fulfil $p_T > 100$ GeV and $|\eta| < 2.5$. The two leading jets are required to satisfy $H_{T2} > 800$ GeV in order to ensure

the full efficiency of the jet trigger and that all jets are contained within the ATLAS inner detector. The measurements of TEEC and ATEEC functions were divided into six ranges in H_{T2}. The Fig. 3.8 and Fig. 3.9 show the TEEC and ATEEC distributions unfolded to particle level in comparison with particle-level MC predictions.

The agreement between data and simulation is for Pythia and Sherpa acceptable but Herwig++ seems to lack in this respect. The PDF sets used in perturbative calculations are the LHAPDF6 packages at NNLO from: MMHT 2014, CT14, NNPDF 3.0 and HERAPDF 2.0. For each PDF set a value of α_S and its uncertainty has been obtained using χ^2 method described in [10]. A demonstration of running α_S can be seen in Fig. 3.10. The results from TEEC fits are marked by red stars and the global fit of the running α_S is depicted by the solid black line with the orange band signifying its uncertainty. The world average from 2016 is marked by green hatched band. The global fit and world average functions are assuming that the strong coupling runs according to the two-loop solution of the renormalization group equation. Agreement between the results of TEEC fit and other experiments is very good, although the experimental uncertainties of the 2012 TEEC fit are smaller than in previous measurements in hadron colliders.

The final result of TEEC fit is:

$$\alpha_S(M_Z) \;=\; 0.1162 \pm 0.0011(\text{exp.})^{+0.0076}_{-0.0061}(\text{scale}) \pm 0.0018(\text{PDF}) \pm 0.0003(\text{NP}).$$

The Fig. 3.11 shows the equivalent results as Fig. 3.10 for ATEEC fit. These results show good compatibility with the rest of the measurement as well as with the world average value.

The final result of ATEEC fit is:

$$\alpha_S(M_Z) \;=\; 0.1196 \pm 0.0013(\text{exp.})^{+0.0061}_{-0.0013}(\text{scale}) \pm 0.0017(\text{PDF}) \pm 0.0004(\text{NP}).$$

CMS

Similar studies have been also undertaken by the CMS collaboration at the LHC. A few examples of such studies are [26], [14] and [13]. The studies [26] and [14] are using 5 fb^{-1} of 7 TeV data from proton proton collisions at the LHC.

The result from [26] is:

$$\alpha_S(M_Z) \;=\; 0.1185 \pm 0.0019(\text{exp.})^{+0.0060}_{-0.0037}(\text{theo}) \tag{3.8}$$

The results from [14] :

$$\alpha_S(M_Z) \;=\; 0.1171 \pm 0.0013(\text{exp.})^{+0.0073}_{-0.0047}(\text{theo}) \tag{3.9}$$

The study [13] is using 19.7 fb^{-1} of 7 TeV data from proton proton collisions at the LHC and the resulting value is:

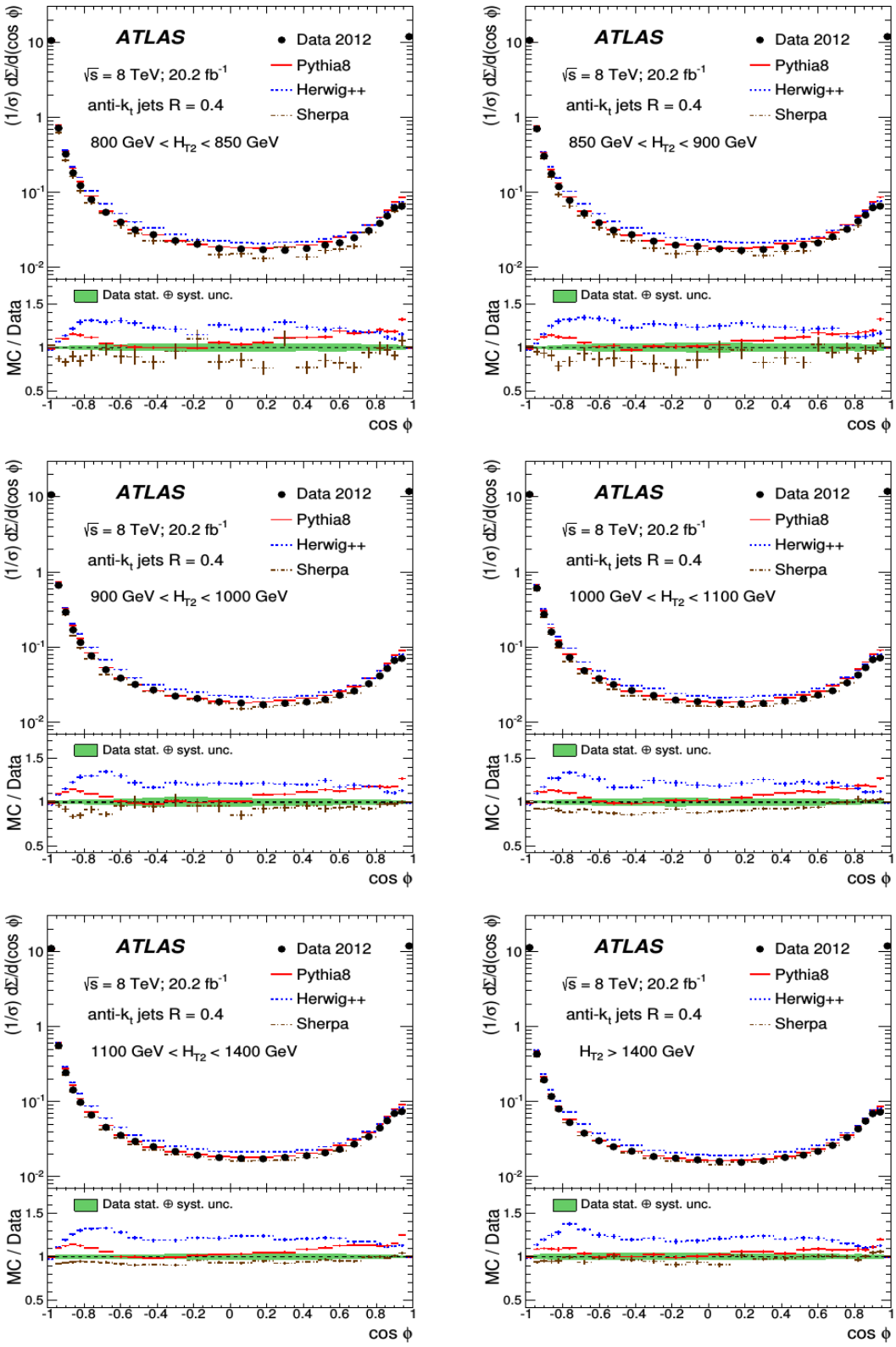

Figure 3.8: The distributions of TEEC in six intervals of H_{T2}. Comparison with MC predictions from Pythia8, Herwig++ and Sherpa. Green shaded bands signify the total uncertainty[10].

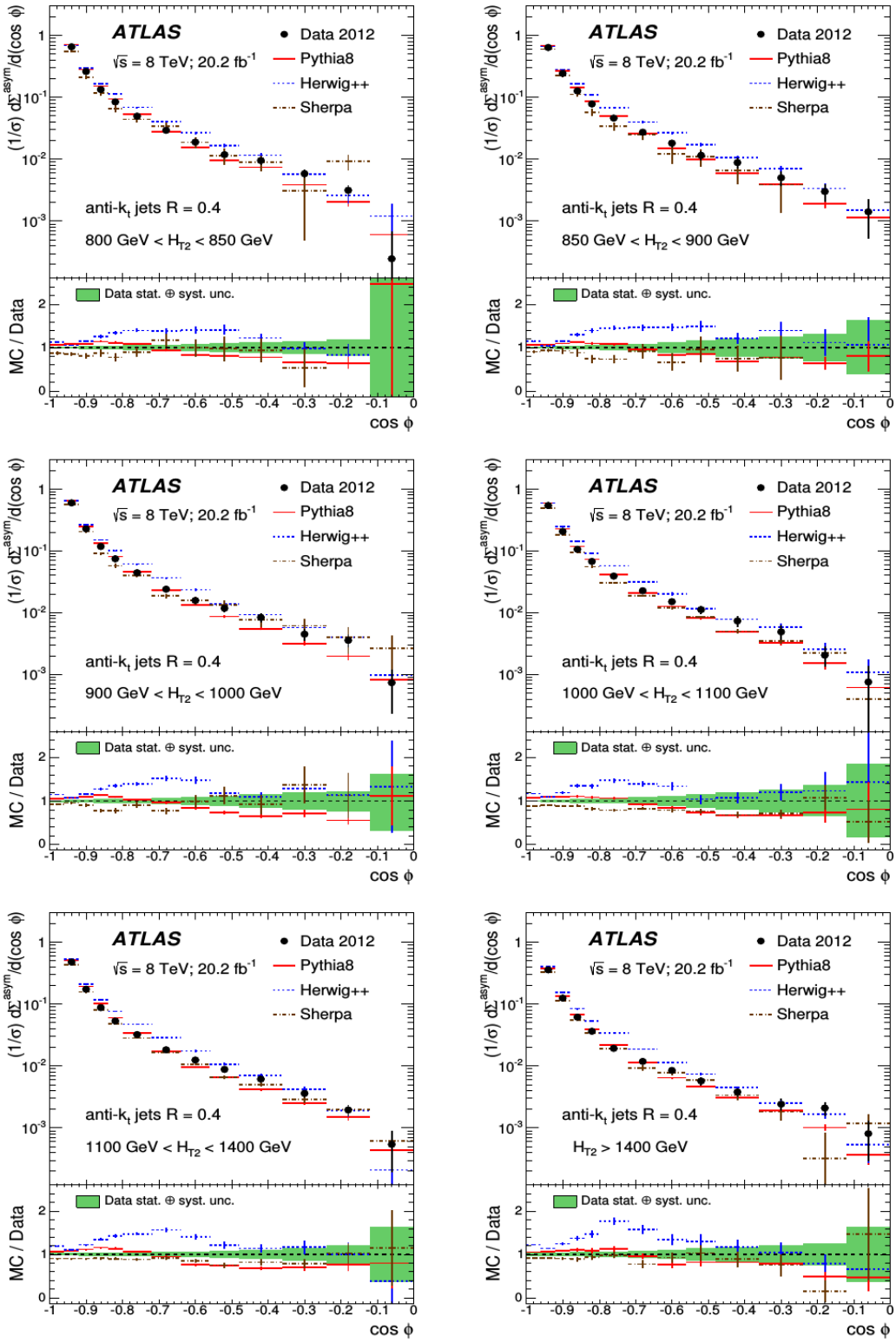

Figure 3.9: The distributions of ATEEC in six intervals of H_{T2}. Comparison with MC predictions from Pythia8, Herwig++ and Sherpa. Green shaded bands signify the total uncertainty[10].

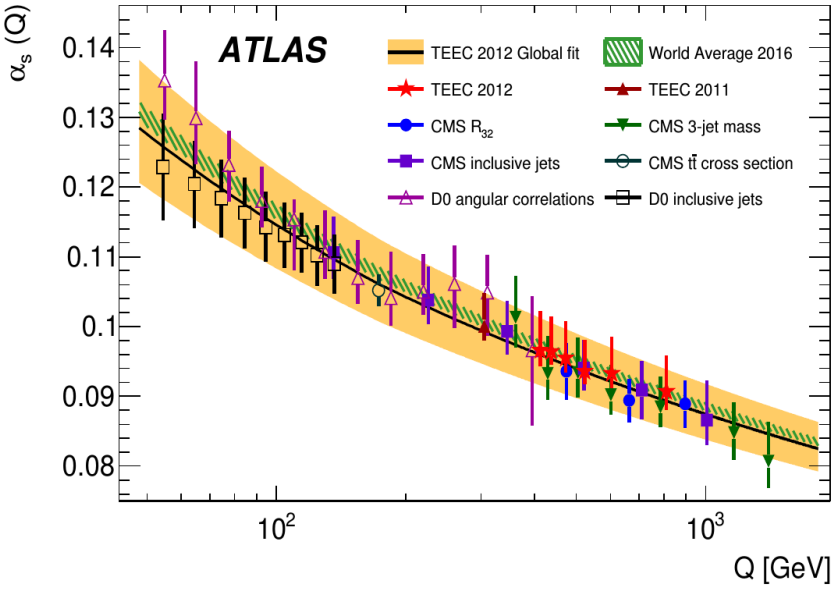

Figure 3.10: The comparison of running $\alpha_S(Q^2)$ values from TEEC fits at the energy scales given by $\langle H_{T2} \rangle/2$ (red stars) with the uncertainty band from the global fit (orange) and the 2016 world average (green band). Results of other experiments are included for better overview[10].

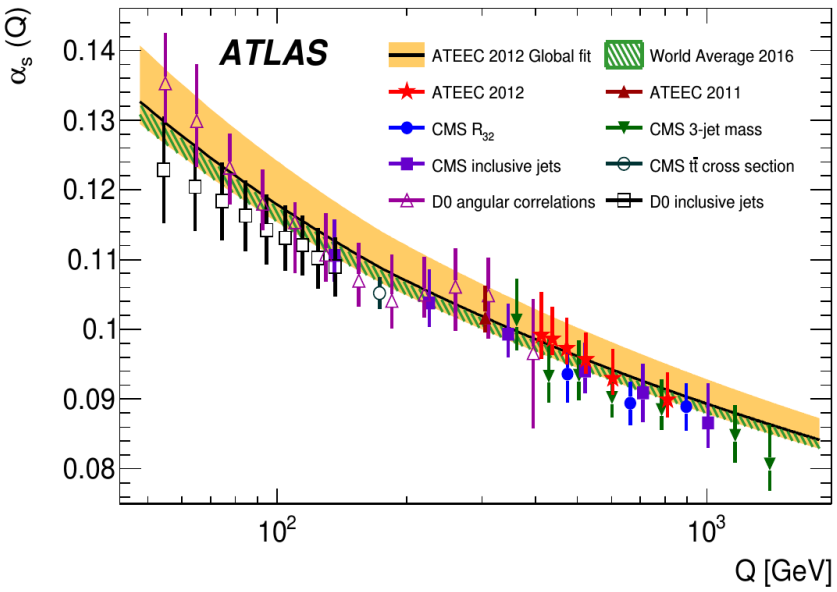

Figure 3.11: The comparison of running $\alpha_S(Q^2)$ values from ATEEC fits at the energy scales given by $\langle H_{T2} \rangle/2$ (red stars) with the uncertainty band from the global fit (orange) and the 2016 world average (green band). Results of other experiments included for better overview.[10]

$$\alpha_S(M_Z) \;=\; 0.1164^{+0.0060}_{-0.0043}. \tag{3.10}$$

3.3.2 Inclusive jet cross-section ratios

Another possible approach to measurement of the strong coupling is from the ratio of the inclusive 3-jet cross section to the inclusive 2-jet cross section. This ratio is proportional to α_S. The CMS collaboration have taken this approach in the study[11]. The analyzed data sample was taken by the CMS detector in the year 2011 at the LHC. The data was from proton-proton collisions wit the centre-of-mass energy of 7 TeV. The integrated luminosity of the data was 5.0 fb^{-1}. The ratio of the inclusive cross sections have been denoted R_{32} and the results of its measurement as a function of the average transverse momentum of the two leading jets $\langle p_{T1,2}\rangle$ can be found in Fig. 3.12 along with NLO predictions for the NNLO PDF sets NNPDF2.1, ABM11, MMSTW2008 and CT10.

The value of $\alpha_S(M_Z)$ resulting from χ^2 minimalization procedure applied to the MC predictions in the region of $(420, 1390)$ GeV is:

$$\alpha_S(M_Z) = 0.1148 \pm 0.0014(\text{exp.}) \pm 0.0018(\text{PDF}) \pm 0.0050(\text{theory}). \tag{3.11}$$

The comparison of the measured values of α_S from R_{32} with results of a few other experiments, along with the global fit of the running coupling and the prediction of the 3-loop solution to the RGE can be found in the Fig. 3.13.

3.3.3 Azimuthal correlation and the quantity $R_{\Delta\phi}$

The study [12] by the ATLAS collaboration measures value of α_S from azimuthal correlation and the quantity $R_{\Delta\phi}$.

The used data are from pp collisions at the LHC at $\sqrt{s} = 8$TeV taken by ATLAS detector during 2012 with the integrated luminosity of 20.2 fb^{-1}. It measures the value of strong coupling constant α_S through testing the quantity $R_{\Delta\phi}$ which is described below. The jets are reconstructed using the anti-k_t algorithm with radius parameter of $R \;=\; 0.6$. The kinematic constraints on the phase space are, that two leading jets have to have transverse momentum $p_T > 100$ GeV and the half of rapidity separation of the two leading jets $y^* < 2$. Another restriction of the dijet phase space is in terms of y_{boost} and y^* so that $|y_{boost}| < y^{max}_{boost} = 0.5$ and $y^* < y^*_{max} = 2.0$. Furthermore, the scalar sum of transverse momenta of all jets that pass the previous cuts is denoted H_T:

$$H_T = \sum_i p_{T,i} \,\text{where}\, \{i \;= jet | (p_{T,i} > p_{Tmin}) \;\wedge\; (|y_i - y_{boost}| < y^*_{max})\} \tag{3.12}$$

and the demand is that the p_T of leading jet satisfies: $p_{T1} > H_T/3$. These constraints are put in place in order to ensure that all the jets are well-measured in the detector

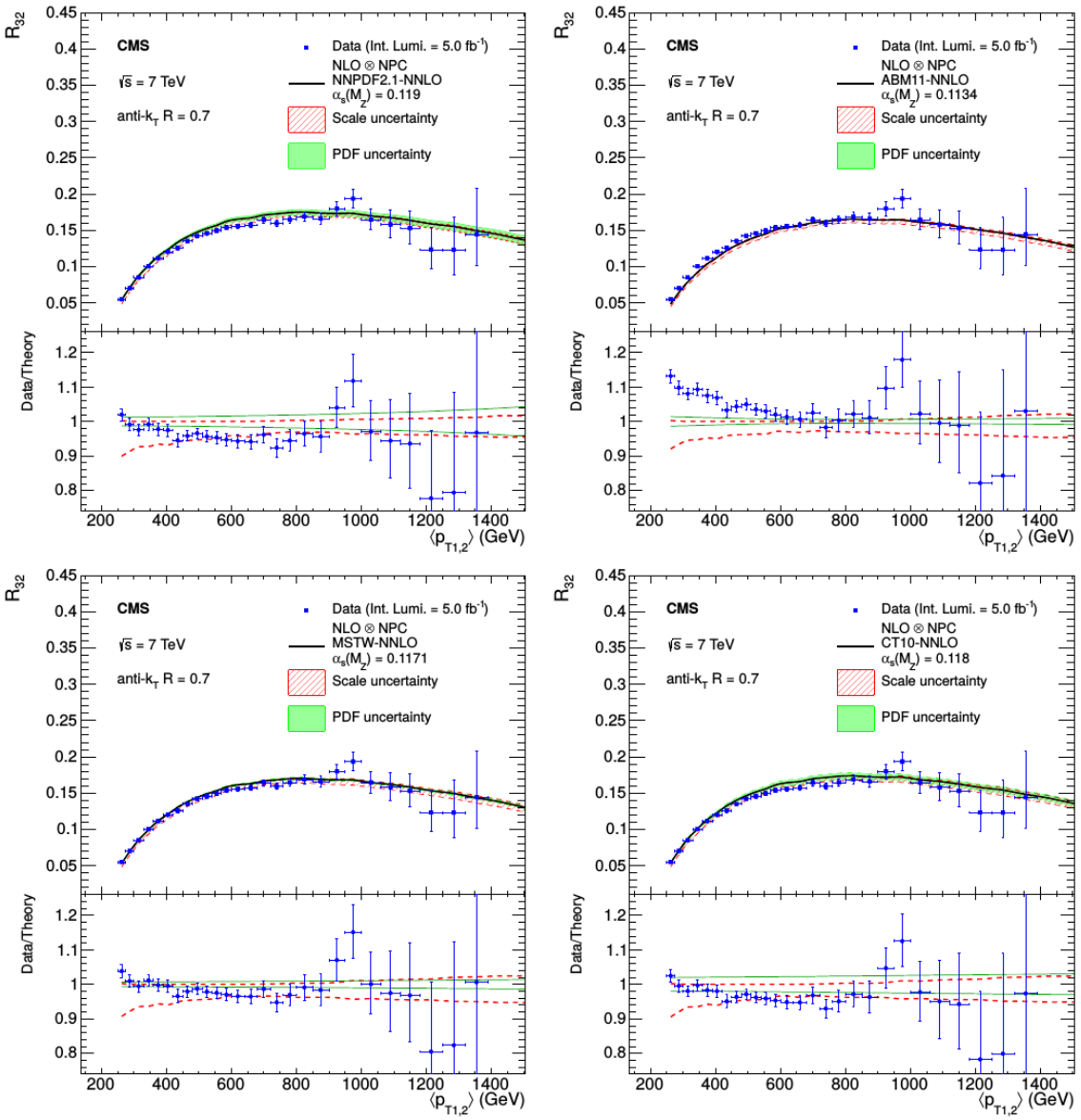

Figure 3.12: Measurement of R_{32} by the CMS collaboration and comparison to NLO prediction using the NNPDF2.1, ABM11, MMSTW2008 and CT10 NNLO PDF sets. Blue points signify data and the solid black line MC prediction [11].

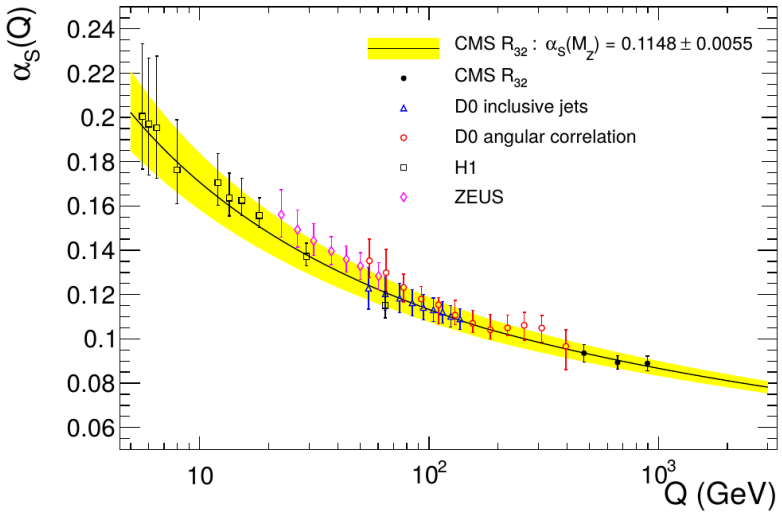

Figure 3.13: The evolution of strong coupling α_S (solid line) with its uncertainty(yellow band) as a function of momentum transfer Q. Determined using 3-loop solution to the RGE with $\alpha_S(M_Z) = 0.1148 \pm 0.0055$. Black dots signify the values of $\alpha_S(Q)$ determined from the measurement [11], the rest of the markers are values of coupling from other collider experiments.

within $|y| < 2.5$ and that contributions from non-perturbative corrections and pileup are negligible. The requirement of $p_{T1} > H_T/3$ is set to reduce the contributions from events with four or more jets and therefore the pQCD corrections from higher orders in α_S.

Quantity $R_{\Delta\phi}$

The quantity $R_{\Delta\phi}$ is then defined in this inclusive dijet event sample as:

$$R_{\Delta\phi}(H_T, y^*, \Delta\phi_{max}) = \frac{\frac{d^2\sigma_{dijet}(\Delta\phi_{dijet}<\Delta\phi_{max})}{dH_T dy^*}}{\frac{d^2\sigma_{dijet}(\text{inclusive})}{dH_T dy^*}} \tag{3.13}$$

The reason behind using $R_{\Delta\phi}$ is to eliminate the effects of PDFs which now cancel out to a large extent and therefore make the ratio specially useful for studies of effect of the strong coupling α_S. The use of $R_{\Delta\phi}$ has been suggested in [27].

The measured results of $R_{\Delta\phi}$ can be found in Fig. 3.14. These results were corrected to the particle level and presented as a fucntion of H_T. At fixed $(y^*, \Delta\phi_{max})$, $R_{\Delta\phi}$ decreases with increasing H_T and increases with increasing y^* at fixed $(H_T, \Delta\phi_{max})$. At fixed (H_T, y^*), $R_{\Delta\phi}$ decreases with decreasing $\Delta\phi_{max}$.

Based on the data points for $\Delta\phi_{max} = \frac{7}{8}\pi$ with $0 < y^* < 0.5$ and $0.5 < y^* < 1$, nine values of strong coupling α_S were determined at scale $Q = H_T/2$ in range $Q \in$

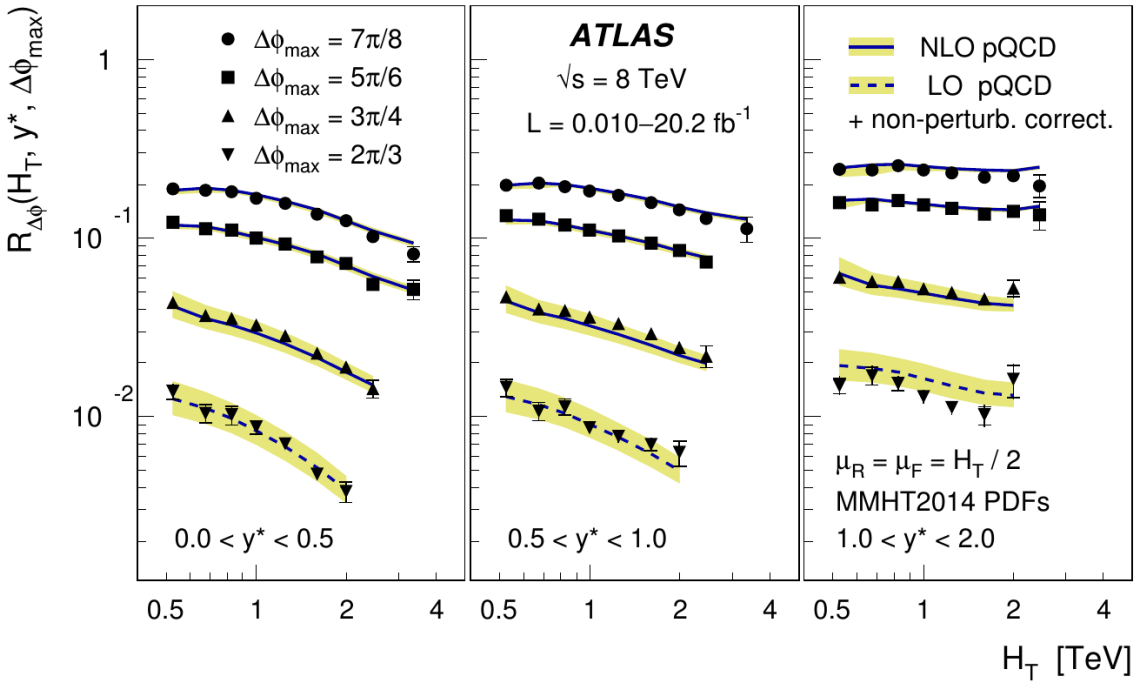

Figure 3.14: The measurement of $R_{\Delta\phi}(H_T, y^*, \Delta\phi_{max})$ as a function of H_T in three y^* regions and four choices of $\Delta\phi_{max}$ [12].

(262; 1675) GeV. The combined analysis results in a value of

$$\alpha_S(M_Z) \;=\; 0.1127\ ^{+0.0063}_{-0.0027}, \tag{3.14}$$

where uncertainty is dominated by the scale dependence of the NLO pQCD predictions.

3.3.4 Summarized results

The results of all the measurements mentioned above are shown in Fig. 3.15 along with the 2018 world average value and its deviation as determined by the particle data group [15]:

$$\alpha_S(M_Z) \;=\; 0.1181 \;\pm\; 0.0011. \tag{3.15}$$

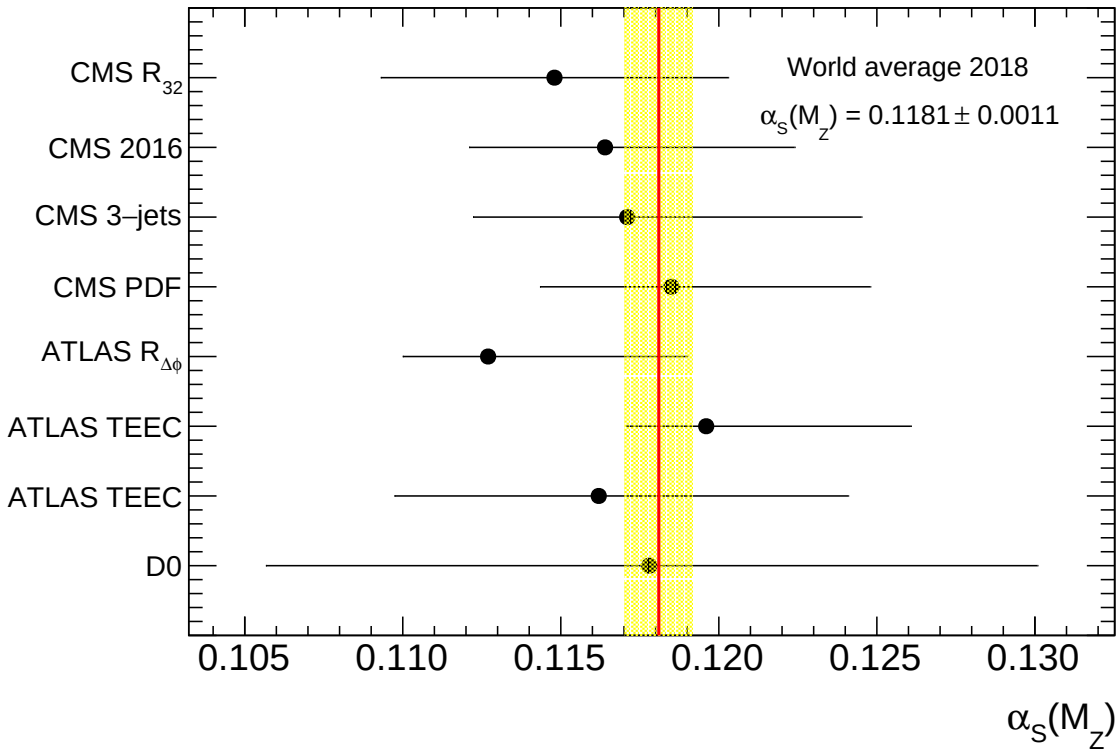

Figure 3.15: The measurement results from [9], [10], [11], [12], [13] and [14] described in this chapter, along with the 2018 world average from [15].

Chapter 4

Analysis

The main concern of this chapter is to provide a first look at data collected by the ATLAS collaboration during the year 2018. The considered data-taking periods are: B, C, D, F, I, K, L, M, O and Q. The total integrated luminosity of the whole data sample corresponding to the unprescaled trigger HLT_j450 used is 58.450 fb^{-1}. Fig. 4.1 shows the delivered and recorded luminosities for the ATLAS detector in 2018 along with the good for physics comparison that corresponds to the luminosity used in this analysis. The unprescaled trigger luminosity of the whole year almost corresponds to the recorded one. The difference is caused by special test runs.

The jets in the data sample are reconstructed using the anti-k_t algorithm with the radius parameter $R = 0.6$. All jets considered in this analysis are required to have $p_T > 100$ GeV in order to eliminate possible jets originating from pile-up, and all jets have to be contained within $|y| < 3.0$ in order to be well measured by the ATLAS detector. In order to be considered an event has to pass at least one trigger described in Tab. 4.1. Each trigger has a p_T range ascribed to it ensuring that it operates in the region of its maximal efficiency. The last column of Tab. 4.1 shows the integrated luminosity taken by its trigger that in turn determines the weight ascribed to the event.

Trigger name	p_T [GeV]	L [pb^{-1}]
HLT_j60	(100, 150)	1.39101
HLT_j110	(150, 230)	20.2962
HLT_j175	(230, 325)	148.101
HLT_j260	(325, 450)	939.19
HLT_j400	(450, 550)	39913.9
HLT_j450	550+	58450.1

Table 4.1: Names of the triggers used in this analysis, their p_T ranges and integrated luminosity L.

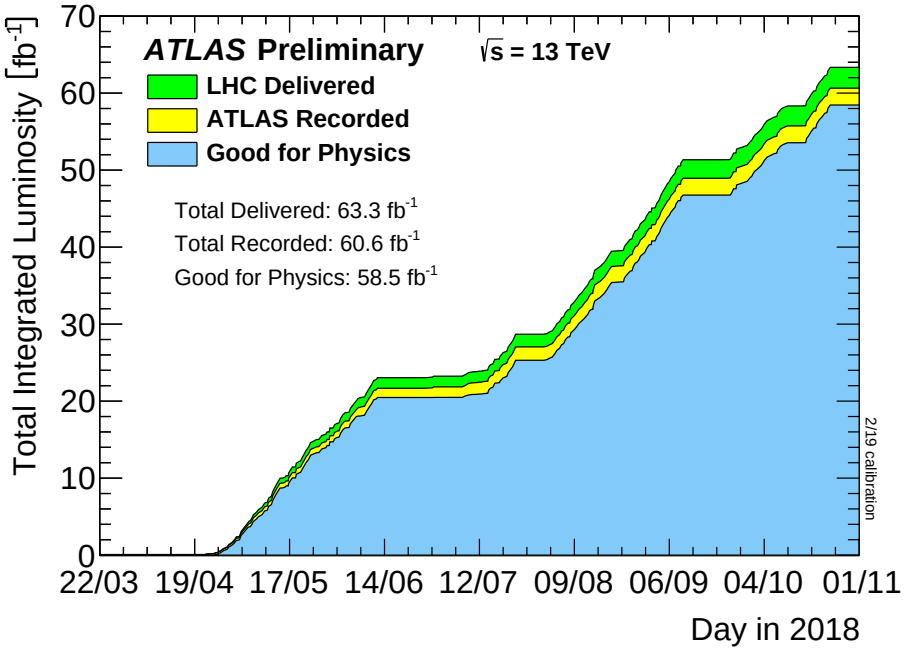

Figure 4.1: The delivered, recorded and good for physics luminosities for the ATLAS detector during the whole 2018 data taking. [16]

The data are compared with MC simulations from LO Pythia 8 with A14 UE tune and PDF set NNPDF2.3 LO, NLO Powheg + LO Pythia 8 shower with A14 UE tune and NNPDF2.3 LO PDF set, and LO Sherpa with NLO external lines and with CT10 PDF set. The MC samples used for comparison are official ATLAS MC based on the mc15 detector simulation routine created by the Standard Model group.

An attempt has been made at creating private MC samples using Herwig 7 and Pythia 8 with the aim to study the effects of α_S variation on the shape of dijet azimuthal correlation. This however, has proven to be unsuccessful due to problems with merging the generated samples, which caused distortions in spectra that far outweighted any possible effects of α_S variation.

4.1 Transverse momentum spectra of inclusive jet production

The first spectrum that is presented from the 2018 data is the spectrum of transverse momentum for the inclusive jet production. It has been measured in six bins of absolute rapidity y shown in Fig. 4.2. The absolute rapidity ranges are: $|y| \in (0.0, 0.5)$, $(0.5, 1.0)$, $(1.0, 1.5)$, $(1.5, 2.0)$, $(2.0, 2.5)$ and $(2.5, 3.0)$. The simulations shown in Fig. 4.2 are scaled in order to match the integrated cross-section of the data. The ratios of the MC spectra to data are shown in Appendix A. The agreement of the MC

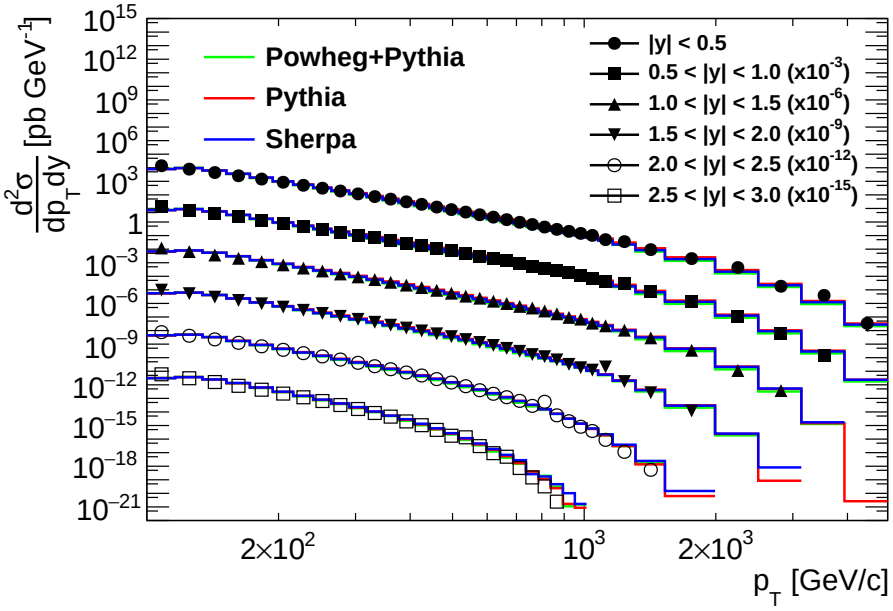

Figure 4.2: Transverse momentum spectra of inclusive jet production shown in six rapidity ranges. Comparison with MC simulations from Pythia 8, Powheg + Pythia and Sherpa. Ratios of MC to Data included in Appendix A

simulations with the data is far from ideal. The overall behaviour is that all the MC models tend to overestimate the measured data in the region below 100 GeV. The normalization then forces the first bin to be below the data. The same effect of normalization can be seen in the tail of the spectra above 100 GeV. Only Pythia alone does not show this significant deviations. Generally speaking we can see up to 40% deviations in shape ignoring the low statistics effects in forward rapidity regions.

Examples of ratio plots are provided in Fig. 4.3a to 4.3c in order to demonstrate the variations in shape of the p_T spectra with inclusive jets in $|y|< 0.5$, for the three generators. The ratio of truth simulation to unfolded data in p_T spectrum is shown in Fig. 4.3d.

The partially successful remedy of the disagreement between the MC and the measured data have been to unfold the data using the bin-by-bin ratio of reconstructed to truth jet p_T from the MC simulations. Histograms of these ratios for the six rapidity ranges are shown in A.5. The results of such unfolding for Powheg+Pythia compared with the data are shown in Fig. 4.4. The unfolding tends to lower the shape variation of the MC to data. Note that the normalization was set at the reco level not for truth. The explicit ratios of Truth-to-Data spectra are shown in Fig. A.4.

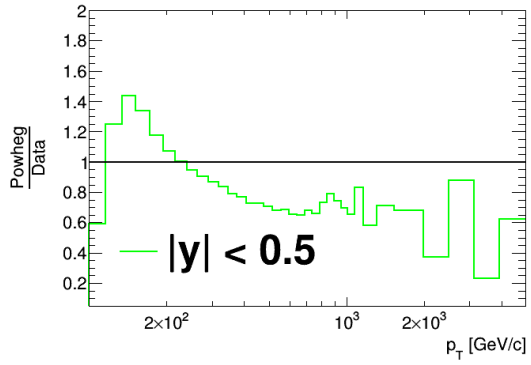

(a) Powheg+Pythia Reco to not-unfolded data shape ratio.

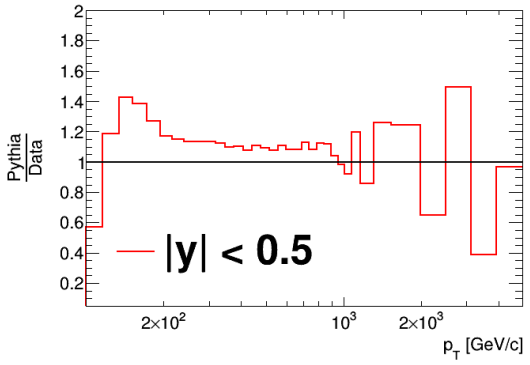

(b) Pythia Reco to not-unfolded data shape ratio.

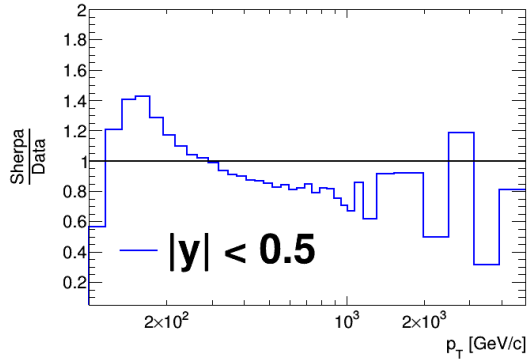

(c) Sherpa Reco to not-unfolded data shape ratio.

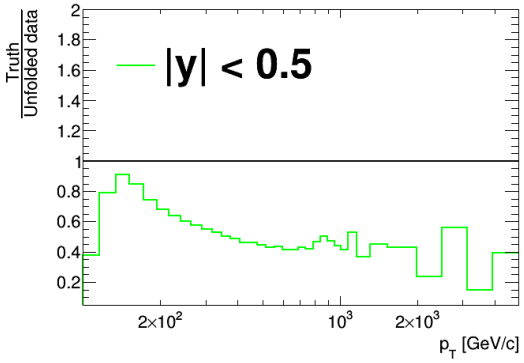

(d) Powheg+Pythia Truth to unfolded data value ratio.

Figure 4.3: Ratio plots of shape variations of Reconstructed spectra to not-unfolded data for different generators (4.3a - Powheg+Pythia, 4.3b - Pythia, 4.3c - Sherpa). Example of ratio of Powheg+Pythia truth spectrum to unfolded data (4.3d).

4.2 Mass spectra of dijet production

The second variable measured in the 2018 data sample is the mass of the leading dijet of each event. There are additional selection criteria for dijet measurements. The first one is that the event is required to have at least two jets. The second one is that the $y^* < 3$. Dijet measurements are divided into six y^* ranges $y^* \in (0.0, 0.5)$, $(0.5, 1.0)$, $(1.0, 1.5)$, $(1.5, 2.0)$, $(2.0, 2.5)$ and $(2.5, 3.0)$. The dijet mass spectrum measured in these ranges is shown in Fig. 4.5 along with a y^* inclusive spectrum and the results of MC simulations as was the case with p_T spectra above. Also similarly to p_T, the MC simulations in Fig. 4.5 are scaled to match the integrated cross section of data and so emphasize the shape variations. In case of dijet mass spectra, the shape agreement is more consistent than transverse momenta as is evident from ratios shown in Appendix B. Most of the ratios stay below 20% deviation in shape. The largest inconsistencies are in the region of dijet mass above 1 TeV.

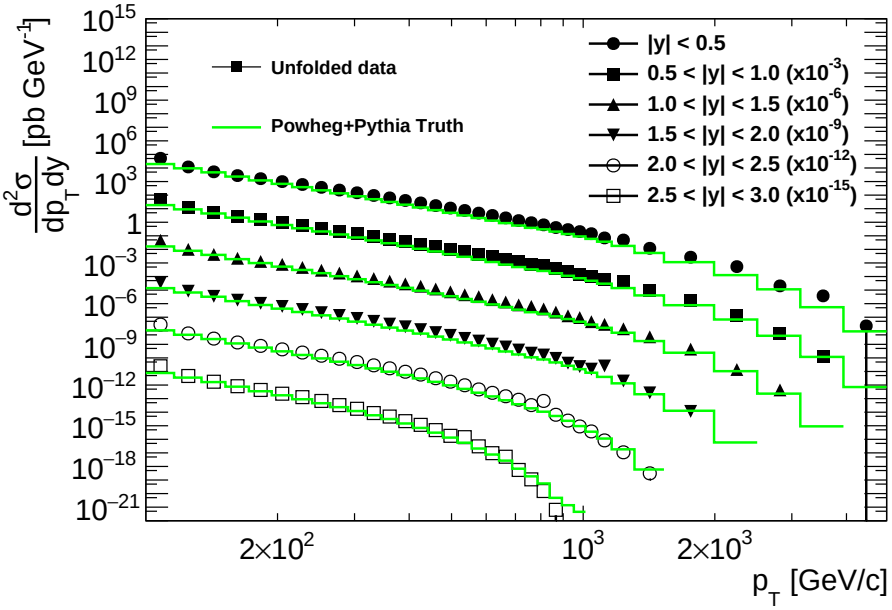

Figure 4.4: Unfolded transverse momentum spectra of inclusive jet production shown in six rapidity ranges. Comparison with Truth MC simulations from Powheg+Pythia. Ratios of MC to Data included in Fig. A.4

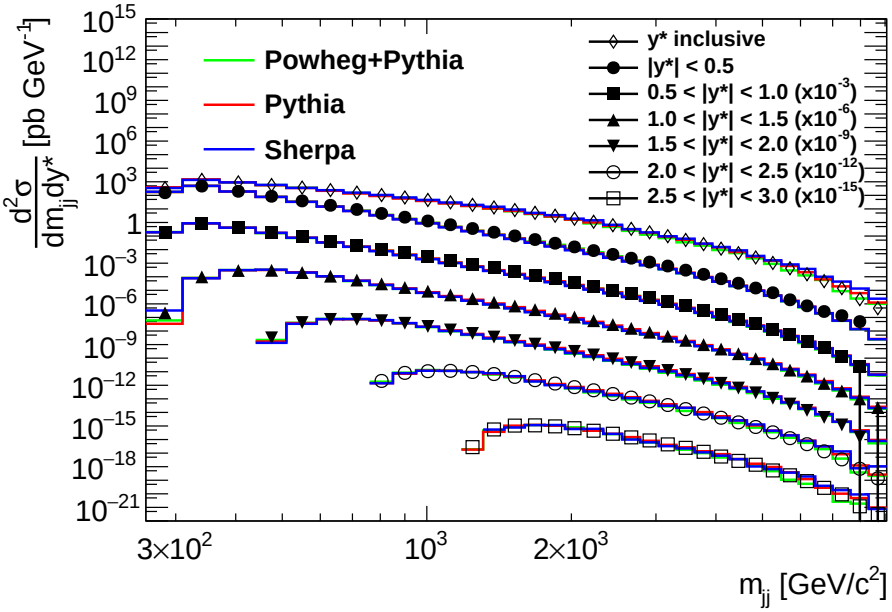

Figure 4.5: Mass spectra of dijet production shown in six y^* ranges. Comparison with MC simulations from Pythia 8, Powheg + Pythia and Sherpa. Ratios of MC to Data included in Appendix B

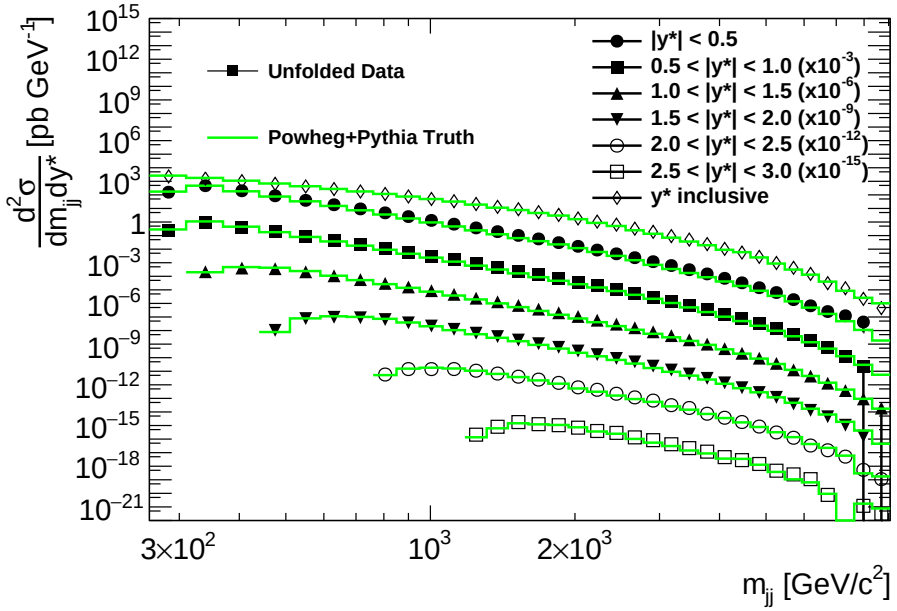

Figure 4.6: Unfolded mass spectra of dijet production shown in six y^* ranges. Comparison with Truth MC simulations from Powheg + Pythia. Ratios of MC to Data included in Fig. B.4

Following the same unfolding logic used with p_T spectra, the Fig. 4.6 shows the comparison of unfolded dijet mass spectra and the truth spectrum from NLO Powheg + Pythia prediction. The unfolding have been done using the ratios shown in Fig. B.5. In this case the unfolding lowers the deviation of the truth mass spectrum prediction from unfolded data in most cases below 20% and does not really change the relative shape deviation. However this agreement is still unsatisfactory due to the low statistical uncertainties of the measured data. This suggests that there is an error in either the analysis and or simulation software used or some hidden effect that comes into play in the 2018 measurement.

The Fig. 4.7a to 4.7c are provided in order to demonstrate the variations in shape of the dijet mass spectra with $y^* < 0.5$, for the three generators. The ratio of truth simulation to unfolded data in dijet mass spectrum is shown in Fig. 4.7d.

4.3 Dijet Azimuthal Correlation

The same selection criteria as for the measurement of dijet mass spectra have been applied during the measurement of the dijet azimuthal correlation. As was the case with dijet mass, $\Delta\phi$ is measured in six ranges of y^* and compared with MC models. The resulting spectra in Fig. 4.8 had to be zoomed to the $\Delta\phi$ range of $(\frac{2\pi}{3}, \pi)$ because below this range the differences between MC models and measured data have become disproportionate even if the spectra have been normalized in order to show only the

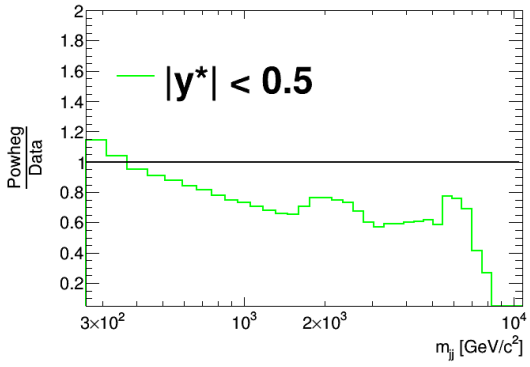

(a) Powheg+Pythia Reco to not-unfolded data shape ratio.

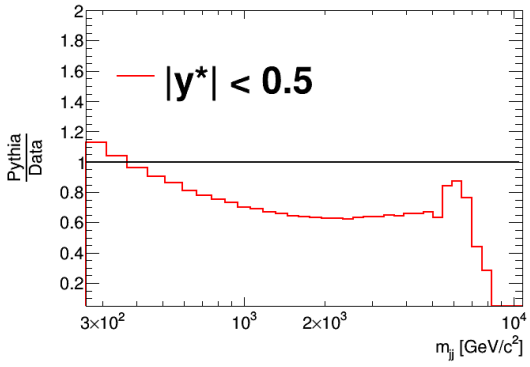

(b) Pythia Reco to not-unfolded data shape ratio.

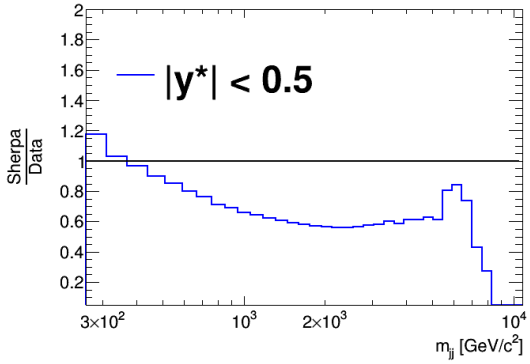

(c) Sherpa Reco to not-unfolded data shape ratio.

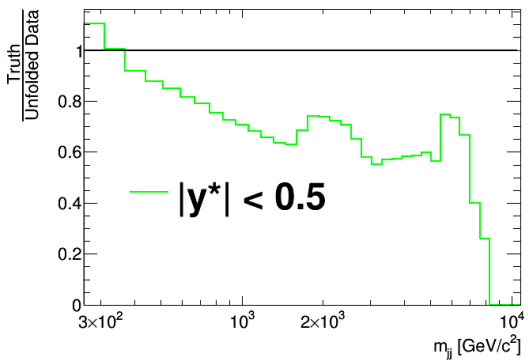

(d) Powheg+Pythia Truth to unfolded data value ratio.

Figure 4.7: Ratio plots of shape variations of Reconstructed spectra to not-unfolded data for different generators (4.7a - Powheg+Pythia, 4.7b - Pythia, 4.7c - Sherpa). Example of ratio of Powheg+Pythia truth spectrum to unfolded data (4.7d).

difference in shape of the spectra. Unfortunately, the results are much worse when it comes to $\Delta\phi$ spectra and so, the unfolding of these spectra and the analysis of the ratios have to be left for future analysis. It is evident from Fig. 4.8, that the only bin, where the MC models describe the data accurately is the last one, which is clearly due to the normalization imposed on the spectra. Towards the lowest boundary, the disagreements are rising and only Pythia is able to contain the disagreement to below that of one order of magnitude, but for example the NLO Powheg+Pythia model differs in some cases by more than 10^4.

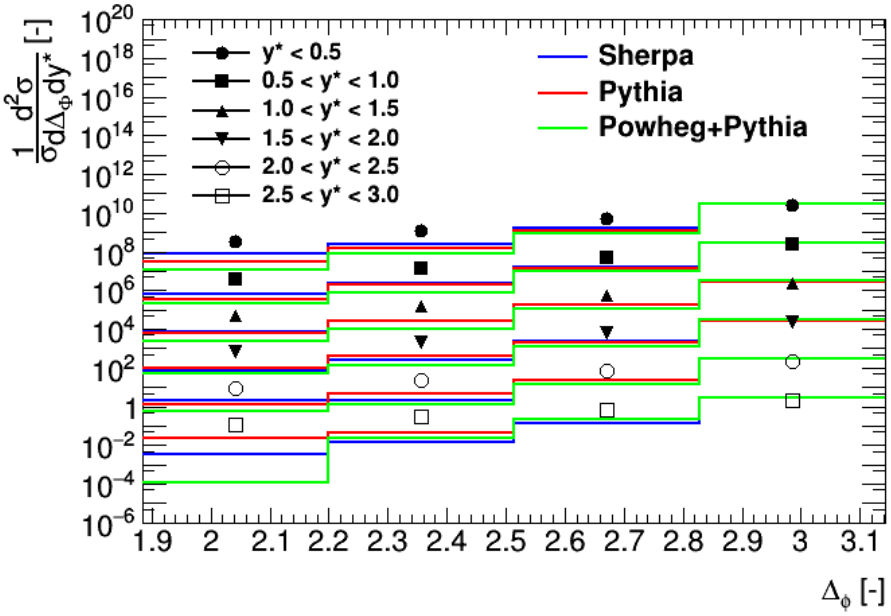

Figure 4.8: The normalized spectra of dijet azimuthal correlation in six bins of y^* in comparison with simulations from Powheg+Pythia, Pythia and Sherpa.

Conclusion

This thesis has been aimed to provide a validation of SM pQCD predictions with the newest data from proton-proton collisions at 13 TeV that was collected by the ATLAS detector during the Run II. The integrated luminosity of the full data sample corresponding to the unprescaled trigger was 58.5 fb^{-1}. The specific goal of this thesis was to measure the dijet angular correlation in proton-proton collisions in the ATLAS experiment. However, the main attention had to be payed to validate newly obtained data sets and to investigate the inclusive jet p_T and dijet mass spectra. Thanks to the large statistics, both observables have been studied doubly differentially with respect to rapidity.

The first and second chapter have been dedicated to providing the necessary minimum of theoretical background in measuring aperture and QCD in order to have a good start for our analysis.

A compilation of previous measurements mainly from ATLAS and CMS experiments have been made in the third chapter in order to have a solid overview of the field of study. It accommodates the measurements of the transverse momentum spectra of the inclusive jet production and the mass spectra of dijet production. A focus is set to overview of studies of azimuthal jet correlations and the α_S extraction.

The analytical part of this thesis deals with the measurement of inclusive jet transverse momentum distributions in six rapidity ranges. The data are compared with MC predictions from three pQCD models: NLO Powheg+Pythia, LO Pythia and LO Sherpa with NLO external lines. The obtained results are considered preliminary since it uses a brand new sample derivations. The overall agreement of MC to 2018 data has shown to be lower than expected. The magnitude of the disagreement goes beyond 20%.

The second part of the analysis presents the measurement of dijet mass in six y^* ranges. The same MC models have been used for comparison with data. In this case the disagreement between simulations and measurement is better, however still not ideal.

The last measurement provided has been the dijet azimuthal correlation. This has been done again in six ranges of y^*. Here, high deviations from data in shape of the spectra for all MC models have been observed, which necessitates a further analysis.

Appendix A

Inclusive jet p_T spectrum

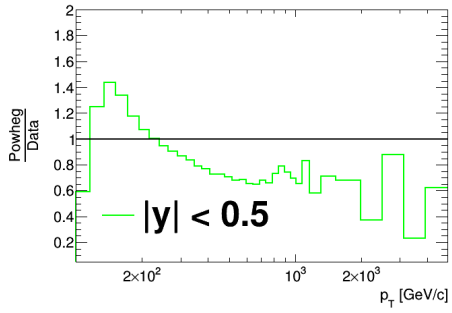

(a) $|y|< 0.5$

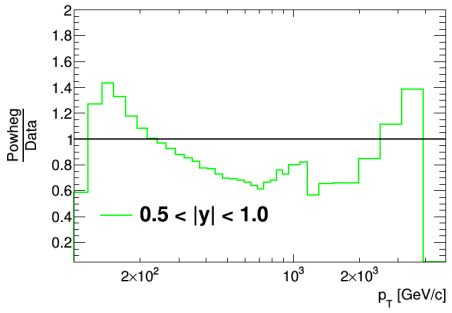

(b) $0.5 < |y|< 1.0$

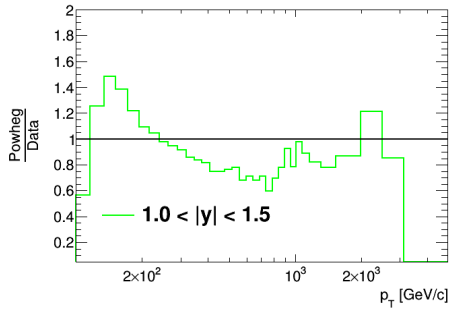

(c) $1.0 < |y|< 1.5$

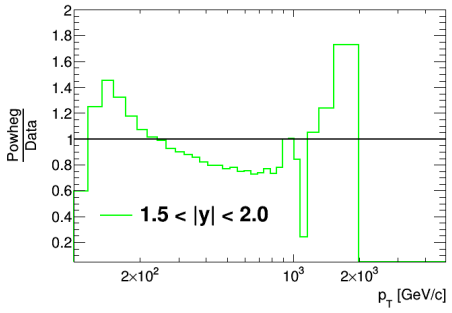

(d) $1.5 < |y|< 2.0$

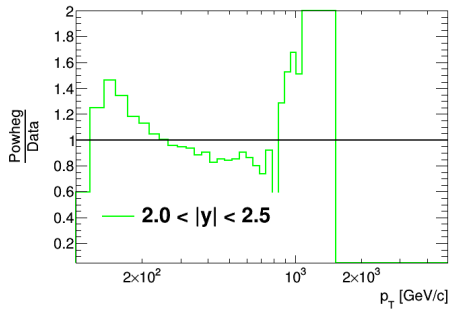

(e) $2.0 < |y|< 2.4$

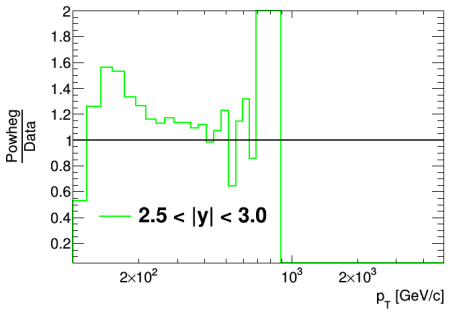

(f) $2.5 < |y|< 3.0$

Figure A.1: Ratios of relative deviation of inclusive jet transverse momentum spectrum shape of Powheg+Pythia simulation from 2018 Data in six ranges of y

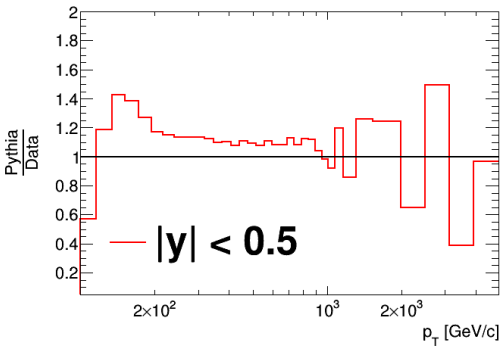

(a) $|y| < 0.5$

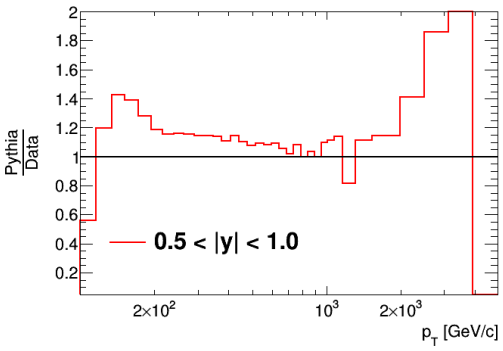

(b) $0.5 < |y| < 1.0$

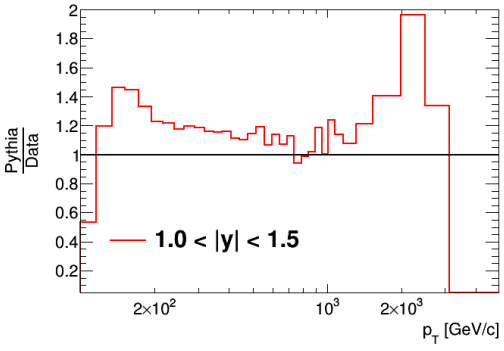

(c) $1.0 < |y| < 1.5$

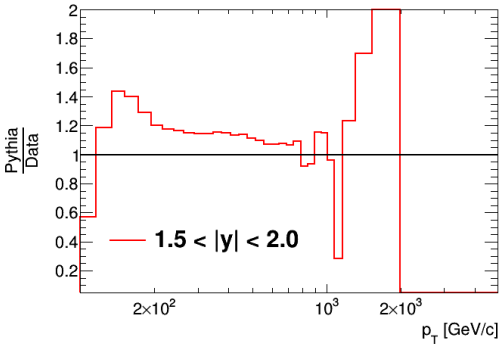

(d) $1.5 < |y| < 2.0$

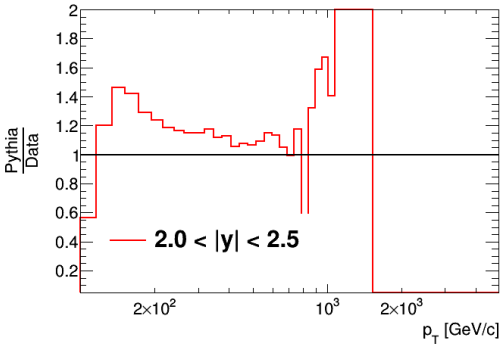

(e) $2.0 < |y| < 2.4$

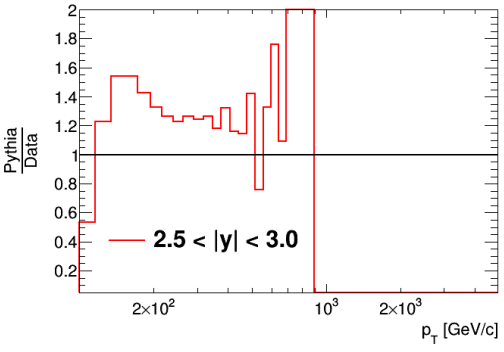

(f) $2.5 < |y| < 3.0$

Figure A.2: Ratios of relative deviation of inclusive jet transverse momentum spectrum shape of Pythia simulation from 2018 Data in six ranges of y

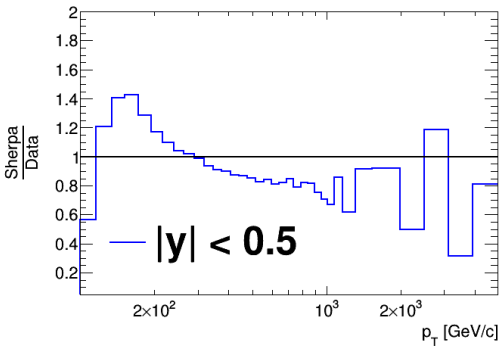

(a) $|y| < 0.5$

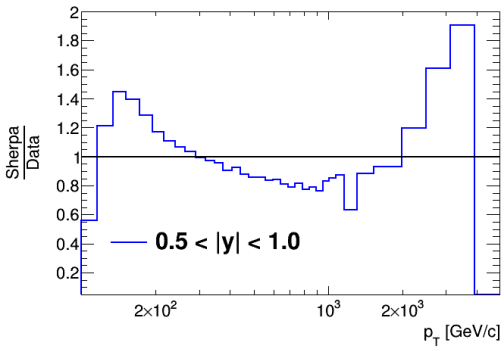

(b) $0.5 < |y| < 1.0$

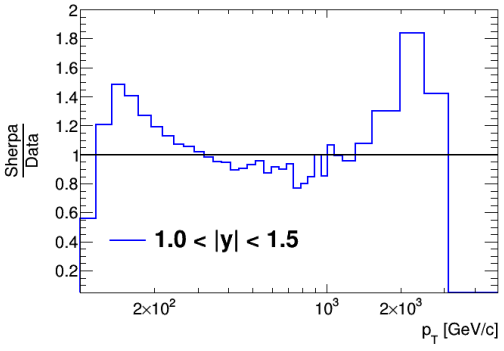

(c) $1.0 < |y| < 1.5$

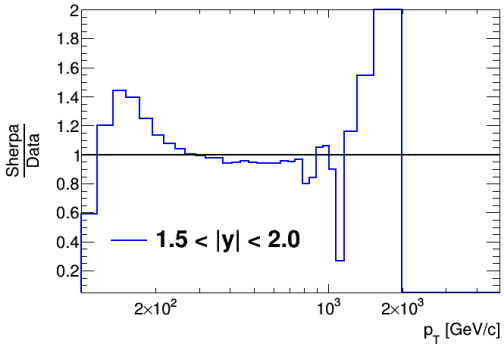

(d) $1.5 < |y| < 2.0$

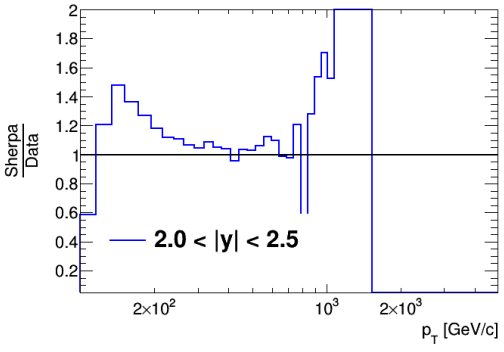

(e) $2.0 < |y| < 2.4$

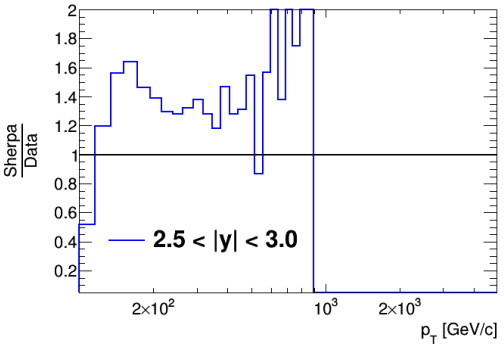

(f) $2.5 < |y| < 3.0$

Figure A.3: Ratios of relative deviation of inclusive jet transverse momentum spectrum shape of Sherpa simulation from 2018 Data in six ranges of y

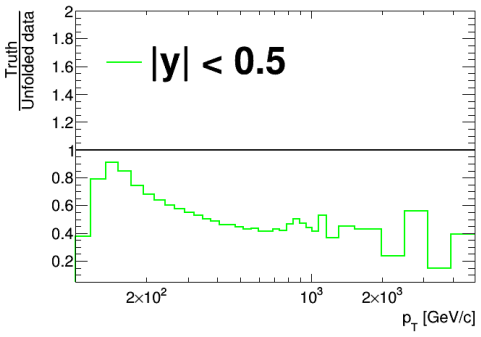

(a) $|y|< 0.5$

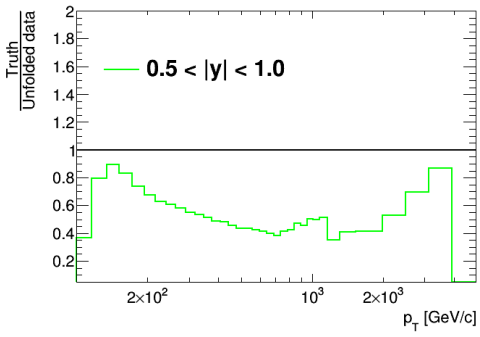

(b) $0.5 < |y|< 1.0$

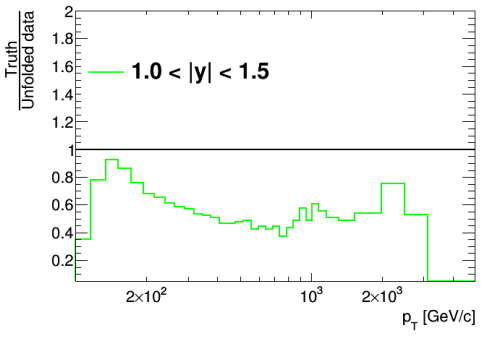

(c) $1.0 < |y|< 1.5$

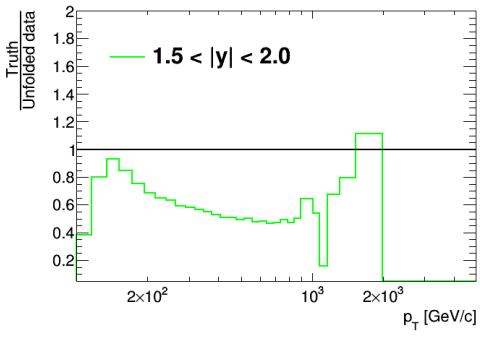

(d) $1.5 < |y|< 2.0$

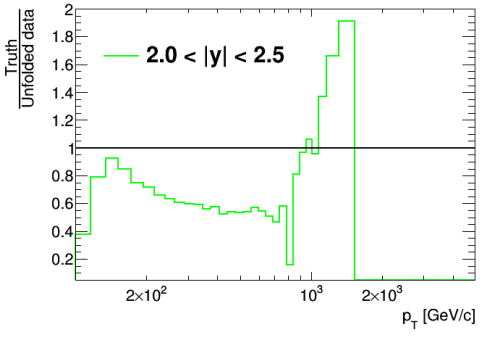

(e) $2.0 < |y|< 2.4$

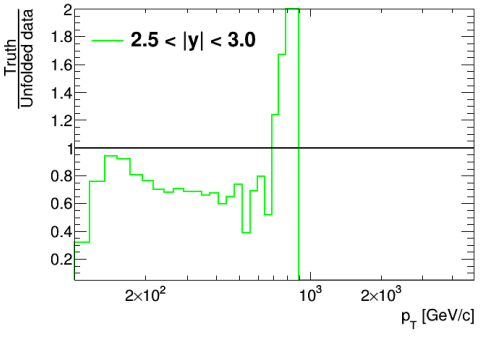

(f) $2.5 < |y|< 3.0$

Figure A.4: Ratios of Truth p_T from NLO Powheg+Pythia spectra to Unfolded data p_T spectra in six ranges of y

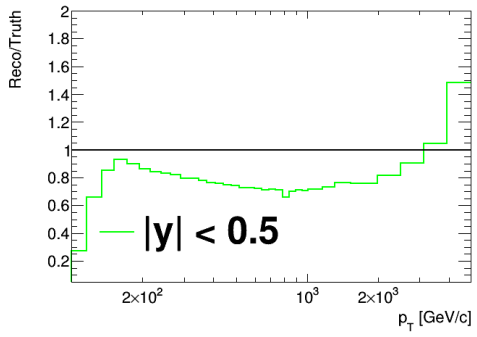

(a) $|y|< 0.5$

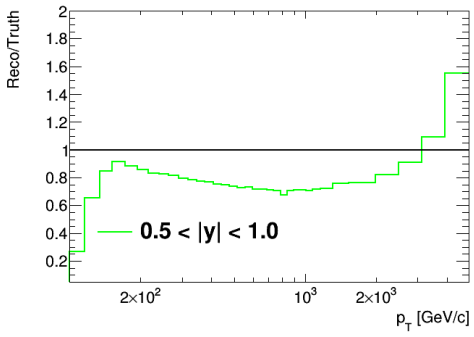

(b) $0.5 < |y|< 1.0$

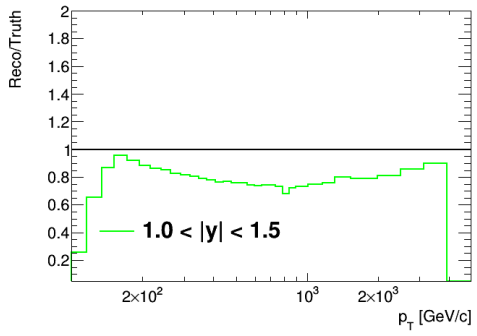

(c) $1.0 < |y|< 1.5$

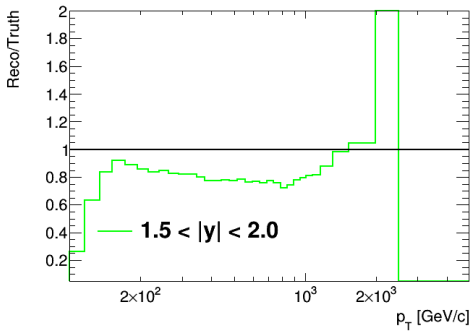

(d) $1.5 < |y|< 2.0$

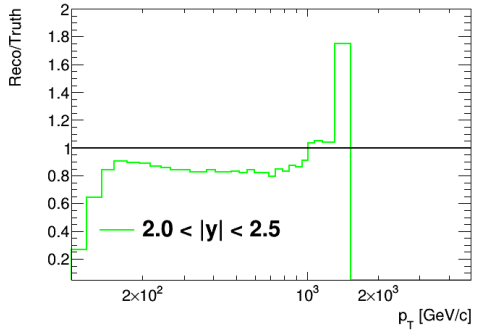

(e) $2.0 < |y|< 2.4$

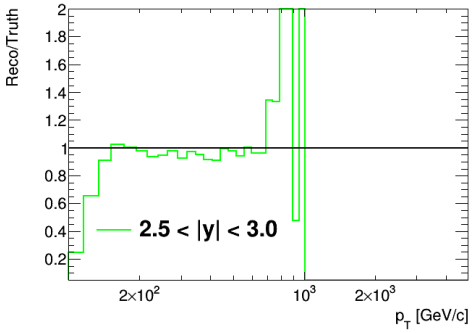

(f) $2.5 < |y|< 3.0$

Figure A.5: Ratios of Reco p_T spectra to Truth p_T spectra from NLO Powheg+Pythia in six ranges of y

Appendix B

Dijet mass spectrum

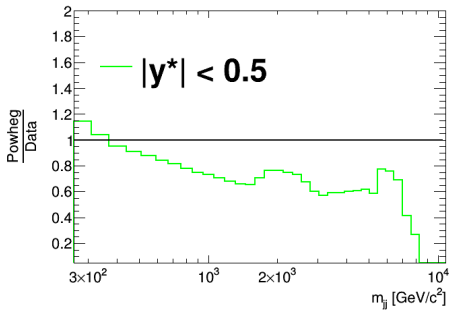

(a) $|y^*| < 0.5$

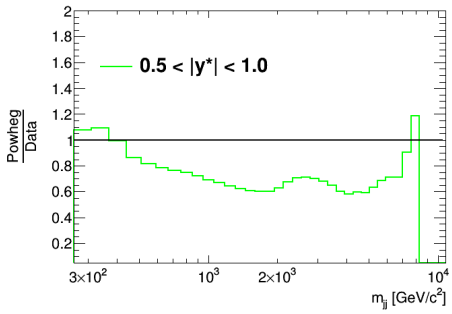

(b) $0.5 < |y^*| < 1.0$

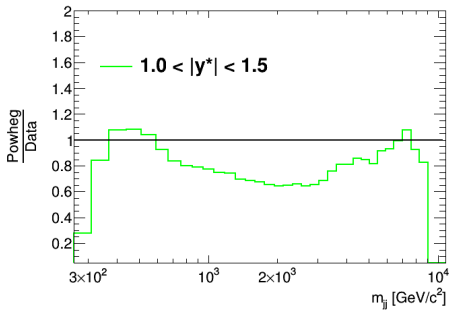

(c) $1.0 < |y^*| < 1.5$

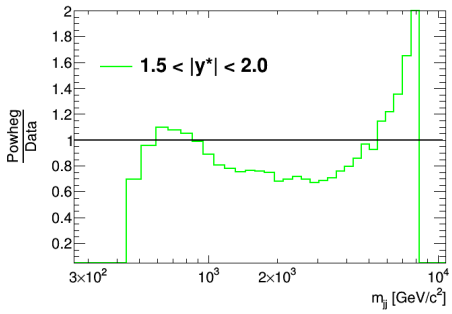

(d) $1.5 < |y^*| < 2.0$

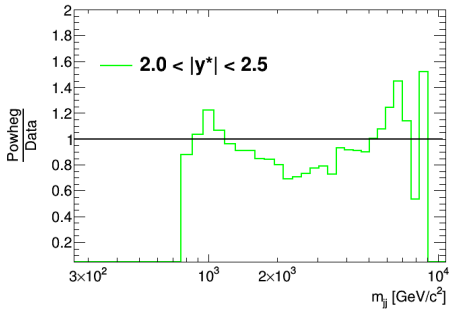

(e) $2.0 < |y^*| < 2.4$

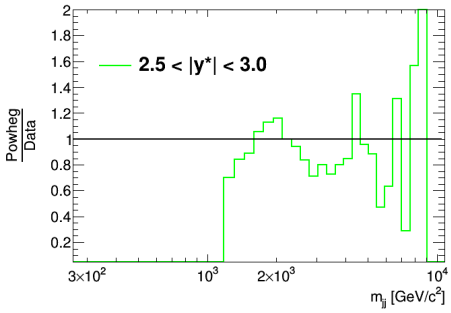

(f) $2.5 < |y^*| < 3.0$

Figure B.1: Ratios of relative deviation of dijet mass spectrum shape of Powheg+Pythia simulation from 2018 Data in six ranges of y^*

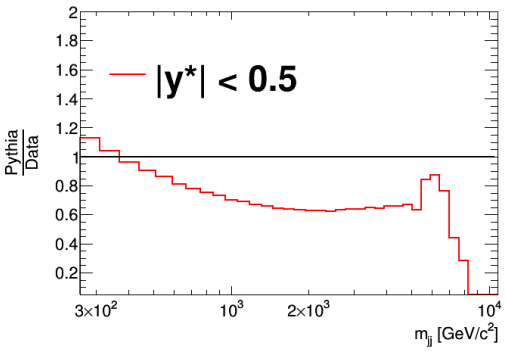

(a) $|y^*| < 0.5$

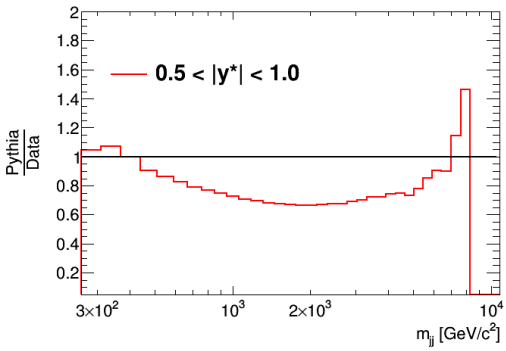

(b) $0.5 < |y^*| < 1.0$

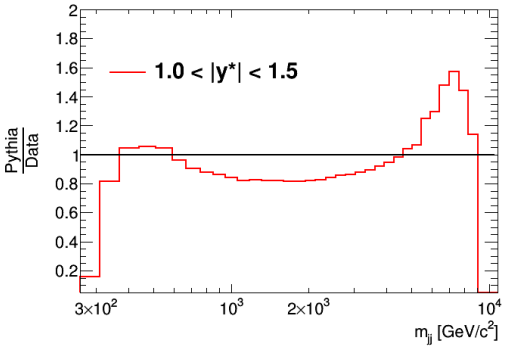

(c) $1.0 < |y^*| < 1.5$

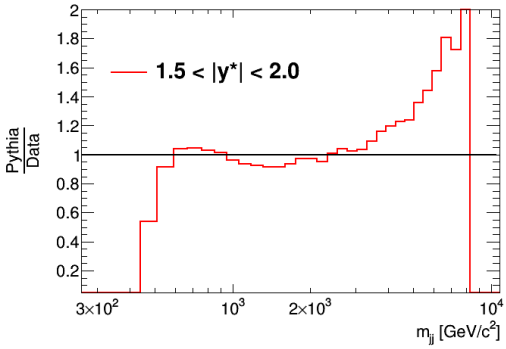

(d) $1.5 < |y^*| < 2.0$

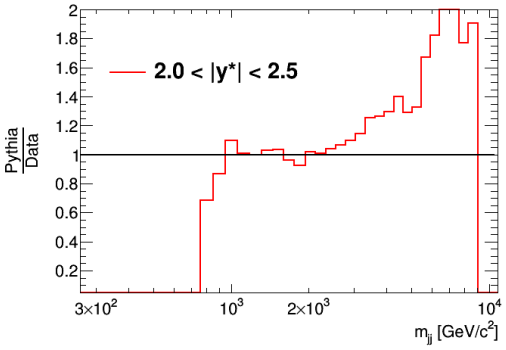

(e) $2.0 < |y^*| < 2.4$

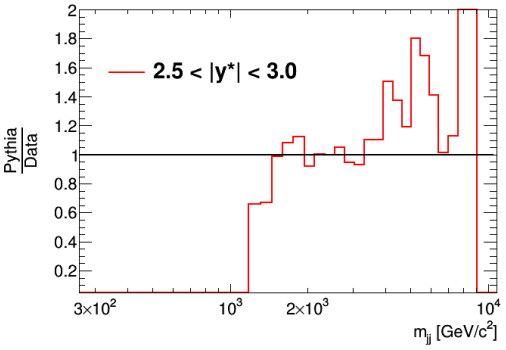

(f) $2.5 < |y^*| < 3.0$

Figure B.2: Ratios of relative deviation of dijet mass spectrum shape of Pythia simulation from 2018 Data in six ranges of y^*

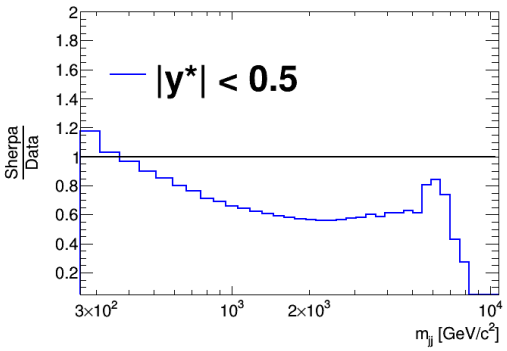

(a) $|y^*| < 0.5$

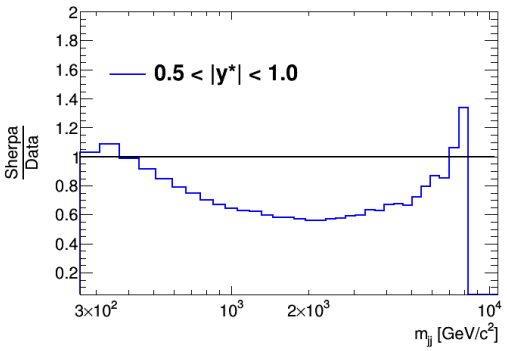

(b) $0.5 < |y^*| < 1.0$

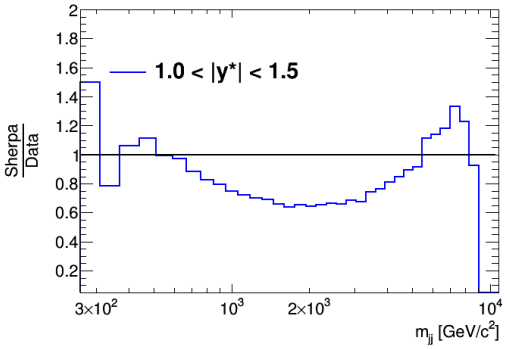

(c) $1.0 < |y^*| < 1.5$

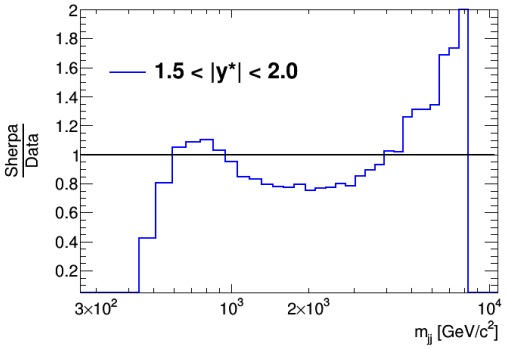

(d) $1.5 < |y^*| < 2.0$

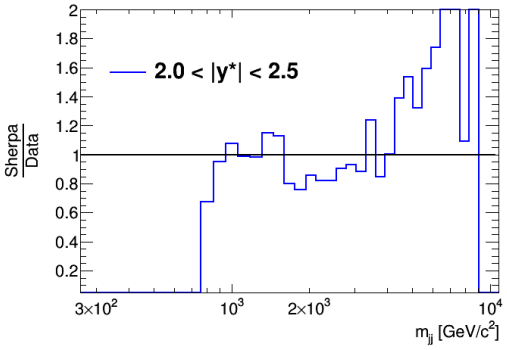

(e) $2.0 < |y^*| < 2.4$

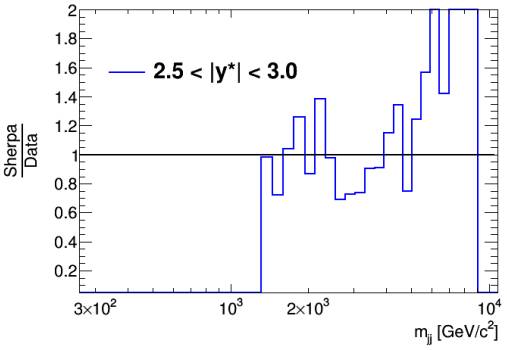

(f) $2.5 < |y^*| < 3.0$

Figure B.3: Ratios of relative deviation of dijet mass spectrum shape of Sherpa simulation from 2018 Data in six ranges of y^*

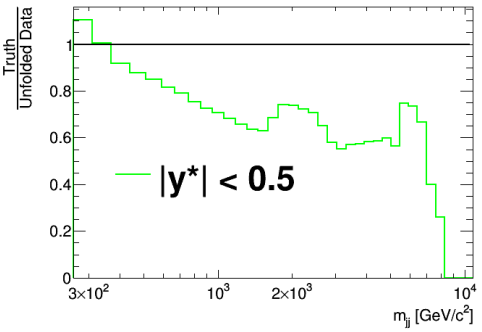

(a) $|y^*| < 0.5$

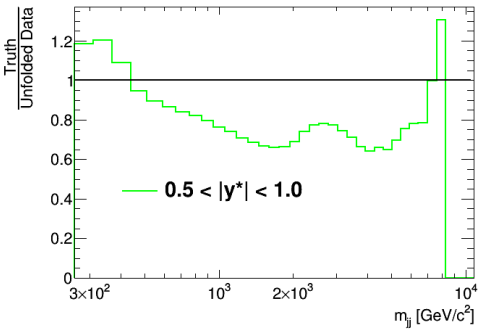

(b) $0.5 < |y^*| < 1.0$

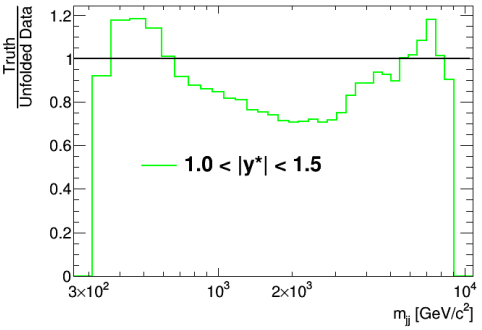

(c) $1.0 < |y^*| < 1.5$

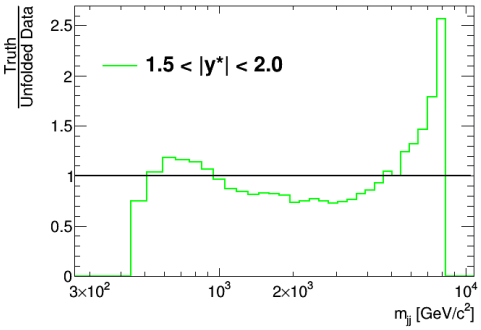

(d) $1.5 < |y^*| < 2.0$

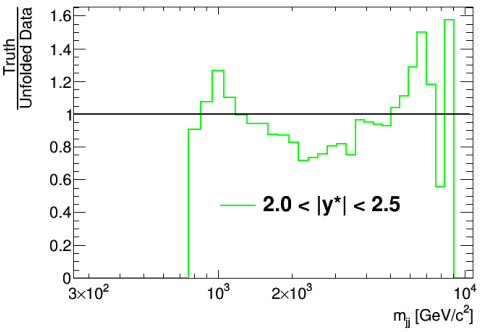

(e) $2.0 < |y^*| < 2.4$

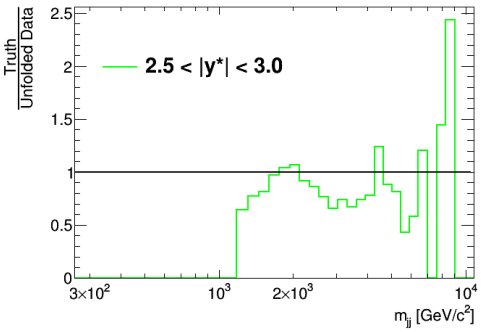

(f) $2.5 < |y^*| < 3.0$

Figure B.4: Ratios of Truth m_{jj} from NLO Powheg+Pythia spectra to Unfolded data m_{jj} spectra in six ranges of y^*

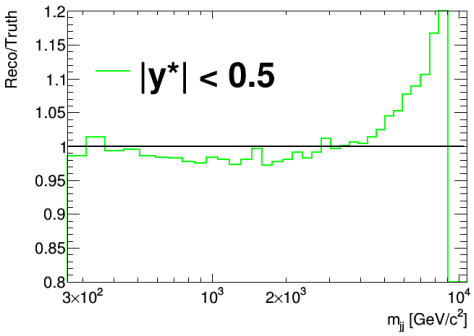

(a) $|y^*| < 0.5$

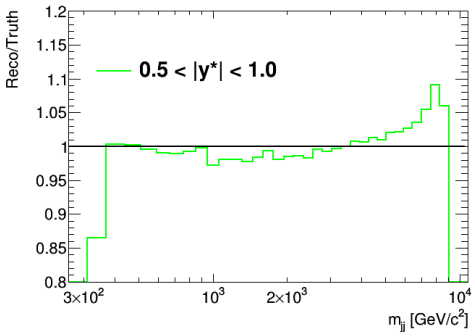

(b) $0.5 < |y^*| < 1.0$

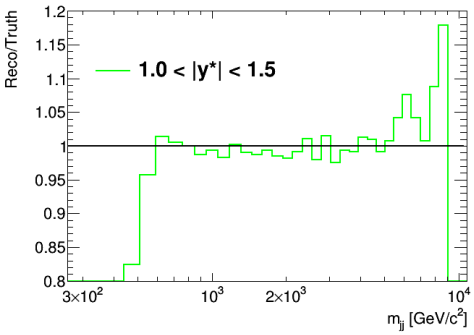

(c) $1.0 < |y^*| < 1.5$

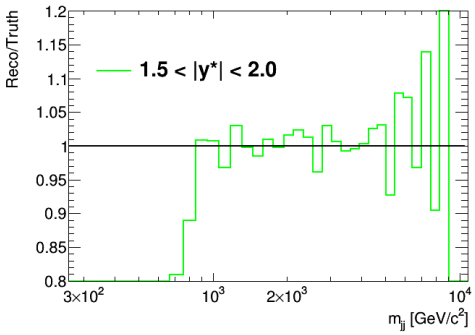

(d) $1.5 < |y^*| < 2.0$

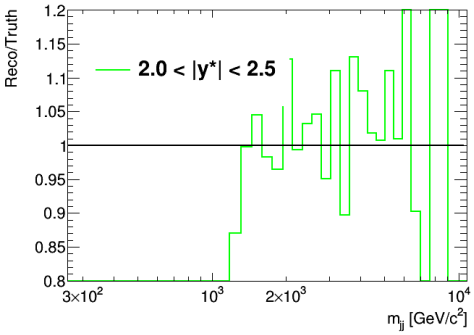

(e) $2.0 < |y^*| < 2.4$

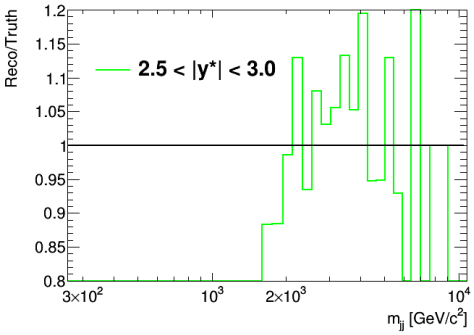

(f) $2.5 < |y^*| < 3.0$

Figure B.5: Ratios of Reco m_{jj} spectra to Truth m_{jj} spectra from NLO Powheg+Pythia in six ranges of y^*

Bibliography

[1] G. Aad et al. The ATLAS Experiment at the CERN Large Hadron Collider. *JINST*, 3:S08003, 2008.

[2] C. Patrignani et al. *Review of Particle Physics. Chin. Phys.*, C40(10):100001, 2016.

[3] Alexandre Deur, Stanley J. Brodsky, and Guy F. de Teramond. *The QCD Running Coupling. Prog. Part. Nucl. Phys.*, 90:1–74, 2016.

[4] M. Aaboud et al. Measurement of inclusive jet and dijet cross-sections in proton-proton collisions at $\sqrt{s} = 13$ TeV with the ATLAS detector. *JHEP*, 05:195, 2018.

[5] M. Wobisch and K. Rabbertz. Dijet azimuthal decorrelations for $\Delta\Phi_{dijet} < 2\pi/3$ in perturbative QCD. *JHEP*, 12:024, 2015.

[6] V. M. Abazov et al. Measurement of dijet azimuthal decorrelations at central rapidities in $p\bar{p}$ collisions at $\sqrt{s} = 1.96$ TeV. *Phys. Rev. Lett.*, 94:221801, 2005.

[7] Vardan Khachatryan et al. Dijet Azimuthal Decorrelations in pp Collisions at $\sqrt{s} = 7$ TeV. *Phys. Rev. Lett.*, 106:122003, 2011.

[8] Georges Aad et al. Measurement of Dijet Azimuthal Decorrelations in pp Collisions at $\sqrt{s} = 7$ TeV. *Phys. Rev. Lett.*, 106:172002, 2011.

[9] V. M. Abazov et al. Determination of the strong coupling constant from the inclusive jet cross section in $p\bar{p}$ collisions at $\sqrt{s} = 1.96$ TeV. *Phys. Rev.*, D80:111107, 2009.

[10] Morad Aaboud et al. Determination of the strong coupling constant α_S from transverse energy–energy correlations in multijet events at $\sqrt{s} = 8$ TeV using the ATLAS detector. *Eur. Phys. J.*, C77(12):872, 2017.

[11] Serguei Chatrchyan et al. Measurement of the ratio of the inclusive 3-jet cross section to the inclusive 2-jet cross section in pp collisions at $\sqrt{s} = 7$ TeV and first determination of the strong coupling constant in the TeV range. *Eur. Phys. J.*, C73(10):2604, 2013.

[12] M. Aaboud et al. Measurement of dijet azimuthal decorrelations in pp collisions at $\sqrt{s} = 8$ TeV with the ATLAS detector and determination of the strong coupling. *Phys. Rev.*, D98(9):092004, 2018.

[13] Vardan Khachatryan et al. Measurement and QCD analysis of double-differential inclusive jet cross sections in pp collisions at $\sqrt{s} = 8$ TeV and cross section ratios to 2.76 and 7 TeV. *JHEP*, 03:156, 2017.

[14] Vardan Khachatryan et al. Measurement of the inclusive 3-jet production differential cross section in proton–proton collisions at 7 TeV and determination of the strong coupling constant in the TeV range. *Eur. Phys. J.*, C75(5):186, 2015.

[15] M. Tanabashi and Others. Review of particle physics. *Phys. Rev. D*, 98:030001, Aug 2018.

[16] ATLAS collaboration. Luminosity public results run 2. 2019.

[17] Richard P. Feynman. *Very high-energy collisions of hadrons. Phys. Rev. Lett.*, 23:1415–1417, 1969. [,494(1969)].

[18] Jerome I. Friedman and Henry W. Kendall. Deep inelastic electron scattering. *Ann. Rev. Nucl. Part. Sci.*, 22:203–254, 1972.

[19] Roel Aaij et al. Observation of the resonant character of the $Z(4430)^-$ state. *Phys. Rev. Lett.*, 112(22):222002, 2014.

[20] Roel Aaij et al. Observation of $J/\psi p$ Resonances Consistent with Pentaquark States in $\Lambda_b^0 \to J/\psi K^- p$ Decays. *Phys. Rev. Lett.*, 115:072001, 2015.

[21] Chris Quigg. *Gauge Theories of the Strong, Weak, and Electromagnetic Interactions.* Princeton University Press, USA, 2013.

[22] Albert M. Sirunyan et al. Measurements of the differential jet cross section as a function of the jet mass in dijet events from proton-proton collisions at $\sqrt{s} = 13$ TeV. *JHEP*, 11:113, 2018.

[23] ATLAS Run 1 Pythia8 tunes. Technical Report ATL-PHYS-PUB-2014-021, CERN, Geneva, Nov 2014.

[24] Gavin P. Salam. Towards Jetography. *Eur. Phys. J.*, C67:637–686, 2010.

[25] Ahmed Ali, Fernando Barreiro, Javier Llorente, and Wei Wang. Transverse Energy-Energy Correlations in Next-to-Leading Order in α_s at the LHC. *Phys. Rev.*, D86:114017, 2012.

[26] Vardan Khachatryan et al. Constraints on parton distribution functions and extraction of the strong coupling constant from the inclusive jet cross section in pp collisions at $\sqrt{s} = 7$ TeV. *Eur. Phys. J.*, C75(6):288, 2015.

[27] M. Wobisch, K. Chakravarthula, R. Dhullipudi, L. Sawyer, and M. Tamsett. A new quantity for studies of dijet azimuthal decorrelations. *JHEP*, 01:172, 2013.

[28] Guido Altarelli. *The Development of perturbative QCD*. 1995.

[29] Vardan Khachatryan et al. Measurement of dijet azimuthal decorrelation in pp collisions at $\sqrt{s} = 8\,\text{TeV}$. *Eur. Phys. J.*, C76(10):536, 2016.

[30] Albert M Sirunyan et al. Azimuthal separation in nearly back-to-back jet topologies in inclusive 2- and 3-jet events in pp collisions at $\sqrt{s} = 13$ TeV. 2019.